

The potential of ALOS PALSAR backscatter and InSAR coherence for forest growing stock volume estimation in Central Siberia



Christian Thiel, Christiane Schmullius

Department for Earth Observation, Friedrich-Schiller University Jena, Loebdergraben 32, 07743 Jena, Germany

ARTICLE INFO

Article history:

Received 6 February 2015

Received in revised form 12 October 2015

Accepted 26 October 2015

Available online 5 November 2015

ABSTRACT

The full potential of ALOS PALSAR L-band interferometric (InSAR) coherence data for the estimation of forest growing stock volume (GSV) in the boreal forest has rarely been investigated. Moreover, ALOS PALSAR backscatter and InSAR coherence have yet to be used together to delineate GSV. Due to the observation strategy and the high acquisition success rate over Eurasia, a large amount of high quality ALOS PALSAR L-band data is available over Siberia. Consequently, this paper investigates the capability of ALOS PALSAR backscatter and InSAR coherence for the estimation of GSV in Central Siberia, Russia. The potential of backscatter and coherence are directly compared using the same inventory data. Altogether, 87 PALSAR images are used and eleven forest inventory sites are investigated.

Based on this large dataset it was observed that InSAR coherence acquired in frozen conditions offers the highest potential for GSV estimation. The saturation level for single coherence images was on average 230 m³/ha, with an average R² between coherence and GSV of 0.58. PALSAR backscatter acquired in unfrozen conditions could also estimate GSV; however, the saturation levels (75–100 m³/ha) and the average R² (0.42–0.48) were lower. HV backscatter offered only a slightly greater potential than HH backscatter.

A simple inversion approach aiming at the delineation of forest GSV maps based on the multitemporal SAR data was developed and applied to five forest inventory sites. This approach combines HV backscatter data acquired in unfrozen conditions and InSAR coherence data acquired in frozen conditions. In general, the produced maps feature a corrected relative RMSE_{corr} of <30% which was similar to the accuracy of the forest inventory data. The R² between inventory data and SAR data based maps varied between 0.54 and 0.83.

© 2015 Elsevier Inc. All rights reserved.

1. Introduction

Much effort is spent on the assessment of the impact of human activities on the climatic change. Main sources of anthropogenic greenhouse gases emissions are from industry, transportation and agriculture. Beside these sources, about 20% of the CO₂ emissions also stem from deforestation or forest degradation (Gullison et al., 2007). Therefore, it is necessary to quantify the amount of carbon bound in living forest biomass or GSV. Due to high temporal dynamics and large forest cover extent, ground based inventories are hardly capable to provide reliable estimates of carbon stock. Additionally, estimations of biomass/GSV from field data can have high uncertainties, as these parameters are typically estimated from field samples, not direct measurements (Saatchi & Moghaddam, 2000). The integration of earth observation (EO) techniques can help to reduce uncertainties as spatial and temporal coverage are improved. EO techniques have already been applied to map forest cover extent, as well as changes in forest cover caused by clear-cut logging and forest fires (Fraser & Li,

2002; Fraser, Li, & Cihlar, 2000; Healey, Cohen, Yang, & Krankina, 2005; Kasischke, Bourgeauchavez, French, Harrell, & Christensen, 1992; Lozano, Suarez-Seoane, Kelly, & Luis, 2008; Rignot, Salas, & Skole, 1997; Thiel, Thiel, & Schmullius, 2009; White, Wulder, Brooks, Reich, & Wheate, 2005; Yatabe & Leckie, 1995). Current EO techniques applied for the estimation of forest stem volume still struggle with problems related to saturation and considerable uncertainties (Dobson et al., 1992; Israelsson, Askne, & Sylvander, 1994; Santoro, Eriksson, Askne, & Schmullius, 2006).

1.1. Radar remote sensing for forest GSV estimation

Many studies have observed a positive relationship between backscatter and biomass/GSV. This association has been successfully simulated by means of simple empirical (Harrell, Kasischke, Bourgeauchavez, Haney, & Christensen, 1997; Lucas et al., 2006; Santos et al., 2003; Smith & Ulander, 1998; Watanabe et al., 2006), semi-empirical (Castel, Guerra, Caraglio, & Houllier, 2002; Kononov & Ka, 2008; Kurvonen, Pulliainen, & Hallikainen, 1999; Luckman, Baker, Kuplich, Yanasse, & Frery, 1997; Santoro et al., 2006; Smith-Jonforsen, Ulander, & Luo, 2005; Sun & Ranson, 2002), and complex physical models

E-mail addresses: Christian.Thiel@uni-jena.de (C. Thiel), C.Schmullius@uni-jena.de (C. Schmullius).

(Disney, Lewis, & Saich, 2006; Israelsson, Ulander, Martin, & Askne, 2000; Kimes, Ranson, & Sun, 1997; Lang, Chauhan, Ranson, & Kilic, 1994; Liang, Moghaddam, Pierce, & Lucas, 2005; Melon, Martinez, Le Toan, Ulander, & Beaudoin, 2001; Nguyen, Roussel, & Tabbara, 2006; Sarabandi & Lin, 2000; Smith & Ulander, 2000; Sun & Ranson, 1995; Ulaby, Sarabandi, McDonald, Whitt, & Dobson, 1990; Varekamp & Hoekman, 2002; Wang, Paris, & Davis, 1998). It is also well-known that radar backscatter can become saturated at low biomass levels; that is, above this biomass level a further increase of biomass causes no further increase of the backscattering intensity. This specific biomass saturation level is determined, among other things, by the radar frequency. Lower frequencies such as L- and P-band are preferable as saturation emerges at higher biomass levels (Carreiras, Vasconcelos, & Lucas, 2012; Joshi et al., 2015; Michelakis et al., 2015; Mitchard et al., 2009; Sandberg, Ulander, Fransson, Holmgren, & Le Toan, 2011; Sandberg, Ulander, Wallerman, & Fransson, 2014; Villard & LeToan, 2015). Other impacts on the saturation level are radar polarisation (Antropov, Rauste, Ahola, & Häme, 2013; Kellndorfer, Dobson, Vona, & Clutter, 2003; Santoro, Eriksson, & Fransson, 2015; Yanasse et al., 1997), forest characteristics (Lucas, Moghaddam, & Cronin, 2004; Lucas et al., 2006), and other general conditions such as weather, soil moisture or surface roughness (Harrell et al., 1997; Pulliainen, Kurvonen, & Hallikainen, 1999; Ranson & Sun, 2000; Santoro et al., 2015; Townsend, 2002).

It has been demonstrated in time series analysis of SAR data that the acquisition date can be optimised for forest biomass derivation (Askne, Santoro, Smith, & Fransson, 2003; Eriksson, Santoro, Wiesmann, & Schmullius, 2003; Koskinen, Pulliainen, Hyyppä, Engdahl, & Hallikainen, 2001; Pulliainen, Engdahl, & Hallikainen, 2003; Santoro, Askne, Smith, & Fransson, 2002). In fact, the integration of many SAR scenes can increase the sensitivity of radar backscatter for forest biomass and the saturation level (Cartus, Santoro, & Kellndorfer, 2012; Kurvonen et al., 1999; Rauste, 2005; Santoro et al., 2011). These positive effects can also be achieved by using multiple radar frequencies and polarisations (Cartus et al., 2012; Del Frate & Solimini, 2004; Harrell et al., 1997; Kellndorfer et al., 2003; Kimes et al., 1997; Neumann, Saatchi, Ulander, & Fransson, 2012; Robinson, Saatchi, Neumann, & Gillespie, 2013).

Besides radar backscatter, InSAR coherence can be utilised for forest parameter mapping (Askne & Santoro, 2005; Eriksson et al., 2003; Gaveau, 2002; Luckman, Baker, & Wegmuller, 2000; Pinto, Simard, & Dubayah, 2012). This approach requires two appropriate SAR images (Askne & Santoro, 2007; Askne et al., 2003; Eriksson et al., 2003). Appropriateness refers firstly to the temporal baseline and the prevailing environmental conditions (e.g., temperature, precipitation, soil moisture, wind speed) (Askne & Santoro, 2007; Askne et al., 2003; Castel, Martinez, Beaudoin, Wegmuller, & Strozzi, 2000; Eriksson et al., 2003; Koskinen et al., 2001; Pulliainen et al., 2003; Santoro et al., 2002; Thiel & Schmullius, 2013), because temporal decorrelation caused by changing environmental conditions can impede the usability of InSAR coherence. In general, very stable conditions, as to be found during the long very cold winters in the boreal zone, can be combined with long temporal baselines (weeks or months). Otherwise, short temporal baselines are preferable (hours to days) (Ackermann, Thiel, Borgeaud, & Schmullius, 2012; Pulliainen et al., 2003; Santoro et al., 2002). In general, temporal decorrelation is larger when shorter wavelengths are used. Although the prediction of temporal decorrelation is extremely challenging, few studies have tried to simulate some components of the temporal decorrelation (Lavalle, Simard, & Hensley, 2012). Secondly, the perpendicular component B_{\perp} of the spatial baseline is of importance (Ackermann et al., 2012; Askne, Fransson, Santoro, Soja, & Ulander, 2013; Askne & Santoro, 2005, 2007; Papathanassiou & Cloude, 2001). As B_{\perp} increases, the amount of geometric and volume decorrelation increases. Moreover, B_{\perp} must not exceed a wavelength dependent critical value, at which all coherence is lost (Gatelli et al., 1994). The geometric decorrelation can be corrected by applying a

range spectral filter (Santoro, Werner, Wegmüller, & Cartus, 2007; Wegmüller, 1998). Thus, the two remaining components that impact the observed InSAR coherence are volume and temporal decorrelation. Over forest, the separation of both impacts is hardly feasible because only single polarisation and single baseline InSAR data are available. One strategy to separate both sources of decorrelation is to either utilise pairs with a zero perpendicular baseline (Ahmed, Siqueira, Hensley, Chapman, & Bergen, 2011; Simard et al., 2012) or a zero temporal baseline. With regard to the latter option, DLR's constellation of TerraSAR-X/TanDEM-X provides and operational data source since 2010. Several studies have already demonstrated the capability of TerraSAR-X/TanDEM-X based InSAR coherence for the retrieval of forest parameters (Ackermann et al., 2012; Askne et al., 2013; Praks, Antropov, & Hallikainen, 2012; Treuhaft et al., 2015; Zan, Krieger, & López-Dekker, 2013).

In a large number of publications a dependency of the magnitude of interferometric coherence on GSV has been emphasised ((IPCC), I.P.o.C.C., 2003; Askne & Santoro, 2005; Askne et al., 2003; Eriksson et al., 2003; Koskinen et al., 2001; Luckman et al., 2000; Pinto et al., 2012; Tansey et al., 2004; Treuhaft et al., 2015). In general, the coherence decreases with increasing GSV. One reason for this relationship is the volume decorrelation which is coupled to GSV (Askne & Santoro, 2005; Askne et al., 2003; Gaveau, 2002). In addition, high GSV promotes temporal decorrelation (Askne & Santoro, 2005; Gaveau, 2002). The relationship between GSV and interferometric coherence has already been described by empirical and physically based models ((IPCC), I.P.o.C.C., 2003; Askne & Santoro, 2005, 2007; Askne et al., 2003; Gaveau, 2002; Pulliainen et al., 2003; Santoro et al., 2002; Sarabandi & Lin, 2000). At optimal conditions saturation occurs at high GSV levels (>300 m³/ha) (Askne & Santoro, 2005, 2007; Koskinen et al., 2001). However, the typical saturation levels are lower (Table 1). Similar to the approaches using backscattering intensities, multitemporal approaches can improve the results (Askne & Santoro, 2007; Askne et al., 2003; Eriksson et al., 2003; Santoro et al., 2002).

1.2. Radar remote sensing in boreal forest

In the boreal zone, the pronounced seasonality needs to be considered when using SAR data (Koskinen et al., 2001; Pulliainen et al., 2003). For example, the trees are typically frozen during the winter. Consequently, a drop of the real part of the dielectric constant ϵ occurs, which results in reduced attenuation, and thus leads to deeper penetration of the electromagnetic (EM) waves into the forest canopy (Kwok, Rignot, Way, Freeman, & Holt, 1994; Way et al., 1990). Hence, the canopy tends to have limited interaction with the EM waves (Way et al., 1994). The reduced attenuation and the deeper penetration impacts backscatter, coherence, and polarimetric signatures. In terms of backscatter, the freezing of forest can cause a drop of more than 3 dB (Dobson, McDonald, & Ulaby, 1990; Kwok et al., 1994; Santoro et al., 2009; Thiel, Thiel, Reiche, Leiterer, & Schmullius, 2007; Way et al., 1990). The sensitivity for GSV is almost lost, and the backscatter difference between forest and non-forest becomes very low (Kwok et al., 1994; Santoro et al., 2015; Thiel et al., 2007; Way et al., 1990). Therefore, radar backscatter is not useful for GSV estimation in frozen conditions.

The general effect of freezing on coherence over forested areas was investigated by a number of studies (Askne et al., 2003; Eriksson, Santoro, & Fransson, 2008; Eriksson, Schmullius, & Wiesmann, 2004; Eriksson et al., 2003; Hagberg, Ulander, & Askne, 1995; Koskinen et al., 2001; Santoro et al., 2002). In stable frozen conditions, coherence was reported less affected by temporal decorrelation. Since the soil is frozen, soil moisture changes do not occur. This results in low temporal decorrelation for open areas. Even large temporal baselines of 44/46 days (JERS-1/ALOS PALSAR) are not necessarily affected by strong temporal decorrelation of non-forested areas (Eriksson et al., 2003; Thiel & Schmullius, 2013). For InSAR pairs with $B_{\perp} > 0$, which is the common case for spaceborne data, the deeper penetration of EM

Table 1
Selection of studies investigating the potential of backscatter and coherence for GSV estimation in European and Asian boreal forest.

Authors	Site	Data	Conditions	Saturation	RMSE	R ²
(Kurvonen et al. (1999))	Southern Finland GSV max = 300 m ³ /ha	JERS-1 L-band (HH) backscatter, 4 scenes; ERS-1 C-band (VV) backscatter, 4 scenes	Diverse unfrozen & frozen	Single images: up to 300 m ³ /ha (defined as GSV class with the highest average backscatter)	Single images: 34.3%–77.1% Multi-temporal: 25%	Single images: 0.01 (ERS-1)–0.42 (JERS-1) Multi-temporal: 0.53
(Rauste (2005))	South-eastern Finland GSV max = 364 m ³ /ha	JERS-1 L-band (HH) backscatter, 6 scenes	Diverse unfrozen & frozen	Single images: 100–200 m ³ /ha (visually estimated) Multi-temporal: >200 m ³ /ha	Multi-temporal: 28.5% (all SAR data combined)	Single images: 0.81 (unfrozen) - -0.05 (frozen) Multi-temporal: 0.85
(Santoro et al. (2006))	Sweden (Kättböle) GSV max = 344 m ³ /ha, Finland (Tuusula) GSV max = 535 m ³ /ha, Siberia (B. Murtinsky) GSV max = 410 m ³ /ha	JERS-1 L-band (HH) backscatter, Sweden: 9 scenes Finland: 3 scenes Siberia: 13 scenes	Diverse unfrozen & frozen	Single images: 100 m ³ /ha (Siberia) – 350 m ³ /ha (Sweden) (visually estimated)	Multi-temporal: 25% (Sweden) 40% (Finland) 33–51% (Siberia)	Multi-temporal: 0.76 (Sweden) 0.68 (Finland) 0.31–0.73 (Siberia)
(Antropov et al. (2013))	2 sites in southern Finland GSV max = 314 m ³ /ha and 425 m ³ /ha	ALOS PALSAR L-band (HH, HV) backscatter, 3 scenes per site	Diverse unfrozen	Single images: 150–200 m ³ /ha (visually estimated)	Multi-temporal: 43%	Multi-temporal: 0.65–0.71
(Eriksson et al. (2003))	Siberia (B. Murt. N) GSV max = 410 m ³ /ha Siberia (B. Murt. S) GSV max = 470 m ³ /ha Siberia (Chunsky) GSV max = 330 m ³ /ha	JERS-1/ERS-1/2 coherence, B. M. N: 6/2 images B. M. S: 6/2 images Chunsky: 5/3 images	Diverse unfrozen & frozen	Single images (JERS): 100–130 m ³ /ha (visually estimated)	Not estimated	Single images (JERS-1): 0.32–0.76 Single images (ERS-1/2): 0.55–0.76
(Askne et al. (2003))	Sweden (Kättböle) GSV max = 335 m ³ /ha	JERS-1/ERS-1/2 coherence, 9/4 images JERS-1 L-band (HH) backscatter, 9 scenes	Diverse unfrozen & frozen	Not estimated	Single images: 36.5 m ³ /ha–140.1 m ³ /ha (JERS-1 backscatter) 35.6 m ³ /ha–151.5 m ³ /ha (ERS-1/2 coherence) 54 m ³ /ha–61.3 m ³ /ha (JERS-1 coherence) Multi-temporal: 30–35% (JERS-1 backscatter and coherence)	Single images (JERS-1 backscatter): 0.64
(Pulliainen et al. (2003))	Southern Finland (Tuusula) GSV max = 539.3 m ³ /ha	ERS-1/2 coherence, 14 images	Diverse unfrozen & frozen	Not estimated	Single images: up to 48%	Single images: 0.00–0.76
(Santoro, Shvidenko, McCallum, Askne, and Schmullius (2007))	Siberia (B. Murt. N) GSV max = 470 m ³ /ha Siberia (Chunsky) GSV max = 470 m ³ /ha	ERS-1/2 coherence, 4–6 images per site	Diverse unfrozen & frozen	Single images: >300 m ³ /ha at optimal conditions (visually estimated)	Single images: 20–25%	Single images: 0.50–0.80

waves causes increased volume decorrelation. Therefore, the contrast between forested and non-forested areas is increased compared to unfrozen conditions (Eriksson et al., 2008). Moreover, the correlation between GSV and coherence improves (Eriksson et al., 2003; Koskinen et al., 2001). From a number of studies it is evident that coherence images acquired in frozen conditions have potential for forest GSV estimation (Askne et al., 2003; Eriksson et al., 2003; Santoro et al., 2002).

In summer, when unfrozen conditions occur, the situation is different. In terms of coherence, major sources of temporal decorrelation are rainfall (changing soil moisture and interception water), wind and growth-related changes (including foliation and defoliation). Also, the water content within the trees is variable in time (Dobson, 1988; McDonald, Zimmermann, & Kimball, 2002). Thus, temporal decorrelation of forest during unfrozen conditions is increased compared to frozen conditions. Therefore, coherence acquired in unfrozen conditions is less suited for GSV estimation (Eriksson et al., 2008). On the other hand, in unfrozen conditions the L-band backscattering intensity was demonstrated to be useful for GSV assessment in the boreal zone (Antropov et al., 2013; Kurvonen et al., 1999; Pulliainen et al., 1999; Rauste, 2005; Santoro et al., 2006).

Table 1 provides an overview on studies investigating the potential of backscatter and coherence for GSV estimation in boreal forests. Included are key parameters such as source and type of SAR data, quantity of acquisitions, acquisition conditions, GSV saturation level, RMSE (estimated vs. reference GSV), and the coefficient of determination R^2 . For example, in (Kurvonen et al., 1999), JERS-1 L-band (HH polarisation, 4 scenes) and ERS-1 C-band (VV polarisation, 4 scenes) backscatter data were used to delineate GSV over a test site in southern Finland with GSV values up to 300 m³/ha. At optimal conditions (Kurvonen et al., 1999) observed no saturation. The GSV class with the highest average backscatter was used to determine the level of saturation. Based on the single images the relative RMSE varied between 34.3% and 77.1%, while R^2 ranged from 0.01 (ERS-1) to 0.42 (JERS-1). Best results were obtained for a combination of all SAR data and the exclusion of small forest stands (relative RMSE = 25%, R^2 = 0.53).

The selected of studies (Table 1) demonstrate that SAR data can potentially support GSV estimation in the boreal forest. Some of these studies also show that the application of multi-temporal data exploration strategies result in improved estimation results. Some of the above studies investigated both, radar backscatter and InSAR coherence. However, examples where both data types are implemented for the delineation of one GSV product are very rare. In this regard the potentially most familiar product is the forest GSV map of Central Siberia produced within the Siberia-1 project (Balzter et al., 2002; Gaveau, 2002; Tansey et al., 2004; Wagner et al., 2003). This map is based on ERS-1/2 tandem coherence and JERS-1 backscatter data acquired in 1997/98. It covers an area of 900,000 km². During the project the team developed a classification strategy that separates the GSV classes <20 m³/ha, 20–50 m³/ha, 50–80 m³/ha, and >80 m³/ha. Accordingly, all areas with medium to high forest density were not distinguished (due to the spread in the GSV-coherence relationship), which is a major drawback for many potential users of this map. Due to gaps in the ERS-1/2 and JERS-1 acquisitions, a production of an area-wide map was not possible. Furthermore, areas of strong topography were masked, as the used ERS-GEC and JERS-1 images were not radiometrically corrected with respect to topography. Errors due to remaining topographic distortions were still propagated onwards. The geolocation accuracy of the processed SAR data suffered from the usage of GTOPO30 DEM data, as SRTM data were not yet available at that time. This matter was even more complicated by the fact that data of two different sensors featuring dissimilar tracks were used.

Another issue being reported by the authors is that some ERS-1/2 tandem coherence acquisitions (ERS-1/2 data were recorded in autumn) were affected by significant rainfall, which resulted in strong decorrelation and a reduced quality of the final map. As no multitemporal data were available, inappropriate images could not be avoided. Another

data related issue was that only L-HH backscatter images were available at that time, which are known to be less sensitive for estimating GSV compared to cross polarised backscatter. The approach of the Siberia-1 project did not allow for the exclusion of areas where both estimators (ERS-1/2 coherence and JERS-1 backscatter) generated dissimilar results. In summary, the Siberia-1 approach features several data related shortcomings, which can be avoided when PALSAR data and SRTM DEM data are used. The proposed approach is also relevant for current and future L-band missions, as it demonstrates the capability of L-band data for the generation of up-to-date GSV maps in boreal forests.

1.3. Objectives and organisation of the paper

Thanks to the sophisticated observation strategy (Rosenqvist, Shimada, Ito, & Watanabe, 2007) and the high acquisition success rate (approximately 80% over Eurasia), a large amount of high quality ALOS PALSAR L-band data is available over Siberia. Consequently, this paper investigates the potential of the PALSAR dataset, including backscatter and InSAR coherence, for GSV mapping in this region. Although a number of L-band based studies exist, the following issues, which are part of this research, have not yet been addressed previously:

- i) Investigation of the potential of ALOS PALSAR HH and HV backscatter for GSV mapping in Central Siberia in frozen and unfrozen conditions,
- ii) Direct comparison of L-band backscatter and InSAR coherence concerning the potential for GSV mapping (frozen and unfrozen conditions) for the same sites,
- iii) Synergistic implementation of backscatter and InSAR coherence (magnitude) from the sensor ALOS PALSAR (temporal consistency and availability of the data) for the generation of maps with continuous GSV values
- iv) Detection and exclusion of areas where backscatter and InSAR coherence generated dissimilar results to improve the accuracy of the final map.

After introducing the study area and data, the SAR data processing and investigation are described. Subsequently the observations based on PALSAR backscatter and coherence are presented (Section 5.1). The statistics of the empirical study are summarised in Fig. 4. In the following Section 5.2 the methods used to predict GSV with L-band SAR data are described. It also presents the results for a selection of forest inventory sites.

2. Study area

The study area is located in Central Siberia, Russia (Fig. 1) and includes parts of the administrative compartments Irkutsk Oblast and Krasnoyarsk Krai. It is sited in the Middle Siberian Plateau, which is characterised by moderate topography, with elevations up to 1700 m in the southern part. The northern part is rather flat with heights of less than 500 m. Mixed taiga forests (birch, pine, fir, aspen, larch, spruce, and cedar) cover approximately 80% of the region. Central Siberia exhibits extreme continental climatic conditions. The yearly amount of precipitation is generally below 450 mm. Most of the precipitation generally occurs between long dry periods during the summer, while most winters are rather dry with average temperatures considerably below 0 °C. The whole territory is characterised by forest cover disturbances caused by forest fires, insect outbreaks and logging. Although logging has decreased by about 75% since political change in 1989, about 100 million m³ of wood are removed in Russia every year (Peterson, Bergen, Brown, Vashchuck, & Blam, 2009), of which 10% are removed in the Irkutsk Oblast. The high impact of wildfires is illustrated by the great forest partition (40–96%) being in some state of post fire succession (Cuevas-González, Gerard, Balzter, &

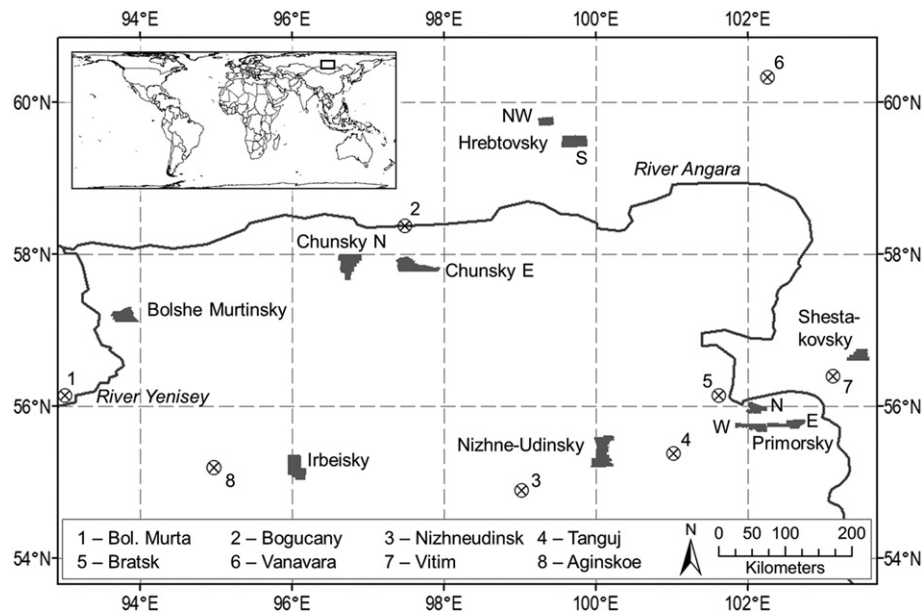


Fig. 1. Study area in Central Siberia including forest inventory sites and weather stations (numbered). Each of the sites contains more than 330 forest stands. All sites together comprise 12,243 stands. Excluding clear-cuts, the average GSV is 185 m³/ha which corresponds to a tree height of 18 m.

Riano, 2009). Forest fires are more common in the light coniferous taiga, dominated by pine and larch. On average, 17,000 large fires (>200 ha) are reported in Russia each year. Insect outbreaks are part of the natural succession and appear cyclically in periods of several years (Baranchikov, 2011). In particular, dark coniferous associations, where fir and spruce dominate, are affected. Once outbreaks appear, very large areas of up to 1 million ha can be infected and destroyed (Baranchikov, 2011).

3. Data

3.1. Forest inventory data

Forest inventory data were available for a number of local sites. This work comprises the sites Bolshe Murtinsky NE, Chunsky N and E, Primorsky N, E, and W, Hrebtovsky S, and NW, Nizhne Udinsky, Irbeisky, and Shestakovsky (Fig. 1, Table 2), as these sites feature a wide range of GSV values (see Table 2), which are relevant for a meaningful empirical data analysis, as well for the training of the empirical models. Each of the sites comprises more than 330 stands. All sites together comprise 12,243 stands. The average stand size is approximately 20 ha with a standard deviation of 11.6 ha. The data contain a multitude of parameters including stand ID, stand age, GSV, and relative stocking. GSV refers to the total volume of tree stems per hectare. It can be converted to dry aboveground biomass (t/ha) by a scaling factor of approximately 1.65 (Håme, Salli, & Lahti, 1992). Note that the GSV values of the inventory data were provided in classes of 10 m³/ha. Clear-cuts have a GSV of 0 m³/ha. Excluding clear-cuts, the average GSV is 185 m³/ha. The data were available in vector format.

In accordance to Russian forest inventory standards, the accuracy of the provided GSV data is 15%–20% relative root mean square error ($RMSE_{inv}$) (Eriksson et al., 2003). Some specific characteristics of the forestry data had to be considered:

- i) Only trees with economic relevance are included (stem diameter > 6 cm),
- ii) High heterogeneity of GSV within forest stands was detected at times (e.g. partly logged),

- iii) Polygons are inaccurate – the misregistration can reach up to 100 m,
- iv) The forest information is about 10 years older (last update in 1998) than the SAR data.

To overcome some of these issues, the following steps were applied:

- i) Buffering the forest stand polygons to avoid errors caused by misregistration (buffer size 100 m, thus 50 m inside and 50 m outside the polygon),
- ii) Excluding forest stands, which have been logged or burned since the last inventory update using recent high resolution KOMPSat and TerraSAR-X satellite data,
- iii) Excluding forest stands <2 ha (loss of 18% of the stands).

3.2. Meteorological data

In Siberia the network of meteorological stations is sparse. The distance between the forest inventory data sites and the corresponding meteorological station can be greater than 200 km. Meteorological data were collected for the stations Bolshaja Murta, Bogucany, Nizhneudinsk, Tanguj, Bratsk, Vanavara, Aginskoe and Vitim (Fig. 1). All meteorological data were gathered from the global World Meteorological Organization (WMO) weather station network. Temperature, precipitation, wind, and snow depth was assembled for the acquisition date of the SAR data. Regarding precipitation, a sum of the past 3 and 7 days prior the acquisition was collected.

In general, during the winter the temperatures were below the freezing point and snow accumulated on the ground. During the summer, the temperatures were above 0 °C. Winter SAR acquisitions featuring thaw were omitted in this work. Thaw was declared, when the minimum temperatures exceeded the freezing point. Thaw/refreeze events in between acquisitions were no exclusion criterion.

At no time was heavy rain reported during the SAR acquisitions. The maximum amount of precipitation was 8 mm per day. At most acquisition dates, no precipitation was observed. With respect to the 7-days sum, rather moderate precipitation was also measured. The 7-days sum was always below 10 mm. Yet, the precipitation data should be

Table 2
Forest characteristics of local sites according to inventory data.

	Size [km ²]	Number of stands	Age of stands [y] (av/med/std./min/max)	GSV [m ³ /ha] (av/med/std./min/max)	GSV [m ³ /ha] histogram, relative occurrence (ordinate) in %	Dominant species (Fraction ≥ 10%)
Bolshe NE	67	1604	96/110/66/0/300	167/190/108/0/450		Fir (31%) Aspen (23%) Birch (15%) Spruce (10%)
Chunsky E	47	1113	95/100/74/0/260	115/90/115/0/430		Birch (29%) Pine (24%) Larch (17%)
Chunsky N	54	1284	97/120/71/0/260	129/150/112/0/470		Pine (21%) Birch (19%) Larch (16%) Spruce (11%)
Hrebtovsky NW	10	339	157/170/54/0/280	191/200/70/0/320		Pine (45%) Larch (37%)
Hrebtovsky S	29	867	154/170/59/0/280	171/190/90/0/420		Larch (40%) Pine (26%) Birch (13%)
Nishne Udinsky	51	2046	89/85/60/0/280	169/190/124/0/470		Birch (41%) Pine (31%) Aspen (12%)
Irbeisky	50	1720	138/160/63/0/260	165/190/111/0/500		Fir (28%) Birch (19%) Cedar (13%) Aspen (12%)
Primorsky E	21	994	105/90/78/0/290	152/180/113/0/500		Pine (34%) Birch (27%)
Primorsky N	15	752	80/83/63/0/200	119/90/98/0/350		Pine (44%) Aspen (22%) Birch (22%)
Primorsky W	18	710	100/80/71/0/260	137/120/100/0/440		Birch (36%) Pine (34%)
Shestakovsky	20	814	107/93/59/0/250	183/210/97/0/380		Pine (26%) Birch (24%) Larch (17%) Aspen (12%)

av = average, med = median, std. = standard deviation, min = minimum, max = maximum.

interpreted with care, as the weather stations are mostly located generally far from the sites (Fig. 1). In particular during summer, when thunderstorm-type precipitation is prevalent, the measurements at the stations are not necessarily related to the precipitation at the local sites. Therefore, based on the available meteorological data the impact of rain cannot be investigated.

Wind data were also collected. As wind conditions can change quickly, the measurement time must not significantly deviate from the SAR data acquisition time. However, in some cases, wind and SAR acquisition differed more than 10 h. Apart from that, the measured wind speeds were mostly close to zero with a maximum of 7 m/s. According to studies (Hagberg et al., 1995) and (Ahmed et al., 2011), wind of this magnitude can be assumed having no or very little impact on L-band

coherence. Thus, in this study it was assumed that the coherence data was not significantly affected by wind.

3.3. ALOS PALSAR data

Table 3 summarises the PALSAR data used in this study. Although the investigation was carried out for 11 local sites, only eight frames were required, as some of the frames cover more than one site. According to the PALSAR acquisition strategy (Rosenqvist et al., 2007), fine beam single (FBS) polarisation data (HH) were acquired in winter (roughly November to March), and fine beam dual (FBD) polarisation data (HH, HV) were acquired in summer/autumn (roughly June to October). Altogether, 87 SLC images were used in this study (FBS: 40 images, FBD: 47

Table 3PALSAR data. *Cursive*: unfrozen; **Bold**: FBD; Other: FBS & frozen, T = track, F = frame.

Location	Chunsky N	Chunsky E	Primorsky	Bolshe	Shesta.	Nizhne	Irbeisky	Hrebt.
Track	T475	T473	T466	T481	T0463	T0471	T0478	T0468
Frame	F1150	F1150	F1110	F1140	F1130	F1100	F1100	F1190
2006		30 Dec 06		28 Dec 06				
2007	<i>20 Jun. 07</i>	14 Feb. 07	18 Jan. 07	12 Feb. 07	13 Jan. 07	11 Jan. 07	10 Aug. 07	6 Jan. 07
	5 Aug. 07	2 Jul. 07	5 Mar. 07	15 Aug. 07	28 Feb. 07	26 Feb. 07	10 Nov. 07	21 Feb. 07
	20 Sep. 07	17 Aug. 07	21 Jul. 07	30 Sep. 07	16 Jul. 07	14 Jul. 07	26 Dec. 07	9 Jul. 07
	5 Nov. 07	2 Oct. 07	5 Sep. 07	31 Dec. 07	31 Aug. 07	14 Oct. 07		24 Aug. 07
	21 Dec. 07	17 Nov. 07	21 Oct. 07		16 Oct. 07			9 Oct. 07
2008	5 Feb. 08	2 Jan. 08	21 Jan. 08	15 Feb. 08	16 Jan. 08	14 Jan. 08	10 Feb. 08	9 Jan. 08
	22 Mar. 08	17 Feb. 08		2 Jul. 08	2 Mar. 08	29 Feb. 08	27 Jun. 08	24 Feb. 08
	7 May 08	4 Jul. 08		17 Aug. 08	17 Apr. 08	16 Jul. 08	12 Aug. 08	11 Jul. 08
	22 Jun. 08	19 Aug. 08			18 Jul. 08	31 Aug. 08	28 Dec. 08	26 Aug. 08
	7 Aug. 08				2 Sep. 08			
2009		4 Jan. 09		2 Jan. 09	18 Jan. 09	16 Jan. 09	12 Feb. 09	11 Jan. 09
		19 Feb. 09		17 Feb. 09	5 Mar. 09	3 Mar. 09	30 Jun. 09	26 Feb. 09
					21 Jul. 09		15 Aug. 09	14 Jul. 09
					5 Sep. 09		30 Sep. 09	29 Aug. 09
					21 Oct. 09			14 Oct. 09

images). For the coherence estimation only the HH polarisation data were used. The azimuth pixel spacing of the SLC data is 3.15 m. The slant range pixel spacing is 4.7 m for FBS (28 MHz), and 9.4 m for FBD (14 MHz) data. Regarding interferogram processing, most image pair combinations were considered. Pairs featuring mixed conditions (frozen and unfrozen), and pairs with B_{\perp} exceeding the critical value were omitted.

As the impact of Faraday rotation (FR) on backscatter and coherence was not corrected (as only single and dual polarisation data were used), a short discussion of potential impacts of FR on the used data is required at this point. FR is the rotation of the polarimetric plane of an EM wave as it interacts with free charges of the ionosphere and the geomagnetic field. The FR angle increases with the total electron content (TEC) and the wavelength of the EM wave. FR becomes negligible, when the angle between the geomagnetic field lines and the radar line of sight (LOS) is 90° (Quegan & Lomas, 2015; Sandberg, Eriksson, & Ulander, 2009). It maximises when LOS and geomagnetic field lines are parallel (Meyer, 2011). Thus, a minimum FR is found at the geomagnetic equator, although the TEC is highest there (Meyer & Nicoll, 2008). The TEC follows some deterministic influences, such as solar zenith angle, day-time, season, solar cycle, atmospheric density profile and geographic location (Meyer & Nicoll, 2008; Wright, Quegan, Wheadon, & Hall, 2003). Global patterns of the FR can be predicted (Wright et al., 2003). However, stochastic processes, such as magnetic storms (regions most affected: auroral zones, polar caps and the postsunset equatorial zone) (Wright et al., 2003), gravity waves, or plasma bubbles (Meyer, 2011) might cause short term regional deviations from the predictions. Besides these stochastic processes, strong FR gradients or irregular patterns can appear at the equator and the auroral zones (Meyer, 2011; Wright et al., 2003). As mentioned above, the magnitude of FR depends on the SAR frequency. While at X-band and C-band FR is negligible, at P-band FR is expected to be strong. At L-band FR effects might become noticeable but are an order of magnitude lower than at P-band (Quegan & Lomas, 2015). In the literature, various magnitudes of FR at L-band are discussed. (Sandberg et al., 2009) assume a maximum FR angle of 45°, which is close to 40° mentioned by (Freeman & Saatchi, 2004). (Wright et al., 2003) estimate a FR angle of 27° at solar maximum and midday (midlatitudes). Several authors claim that when data is acquired at night during solar minima the FR can be neglected in the L-band (Quegan & Lomas, 2015; Rignot, 2000; Sandberg et al., 2009; Wright et al., 2003). In fact, (Meyer & Nicoll, 2008) report that although many thousands of PALSAR scenes are archived, only few images with a predicted FR angle >3° were found. Also, in their study they (Meyer & Nicoll, 2008) estimated the FR for several polarimetric PALSAR images acquired over various regions and seasons. For most of the images the

FR angle was below 2°. The authors provide one example for an area close to the geomagnetic North Pole. The average FR angle for this extreme case was 3.8°. (Sandberg et al., 2009) conducted a similar investigation for a forest site in Sweden (58°30'N, 13°40'E). The maximum FR angle was 3°. The corresponding PALSAR scene was acquired at descending orbit, i.e. during day time. The maximum FR angle for all night time acquisitions (which was the standard in PALSAR's operational phase) was 2.4° (2006, June 3). (Sandberg et al., 2009) and (Meyer & Nicoll, 2008) found a linear relationship between FR predicted from TEC and FR estimated from PALSAR data.

FR impacts backscatter, interferometric and polarimetric parameters (Meyer & Nicoll, 2008). The magnitude of the impact depends on the magnitude of FR. When repeat pass InSAR systems are used, the temporal variability of FR needs to be considered (Rignot, 2000). In terms of L-band backscatter, FR causes a decrease of co-polarised amplitudes and an increase of cross-polarised amplitudes for FR angles up to 40° (Freeman & Saatchi, 2004; Wright et al., 2003). In addition, the dynamic range of the cross-polarisation amplitudes slightly decreases, while the dynamic range of co-polarisation amplitudes slightly increases (Freeman & Saatchi, 2004). If the two images of an InSAR pair are acquired at dissimilar ionospheric conditions, InSAR coherence is decreased (Freeman & Saatchi, 2004; Meyer, 2011; Rignot, 2000).

According to the measurements by Sandberg et al. (2009) and (Meyer and Nicoll (2008)), it is reasonable to assume that the FR in our study is below 5°. All images were acquired at night time and during a solar minimum. In fact, the last solar minimum was lasting longer than expected (NASA, 2014). In 2008 and 2009, a historically low level of sun spots and solar flares was observed. The solar activity slightly increased in 2010, reaching its maximum in 2014, albeit this recent solar maximum is one of the weakest recorded (NASA, 2014). For a FR angle of 5° (Freeman & Saatchi, 2004) estimated an increase of L-HV backscatter of 0.3 dB (forest) to 0.7 dB (bare soil, pasture) and a maximum decrease of L-HH backscatter of 0.1. In their example, the dynamic range of L-HV slightly decreased from 12.2 dB to 11.5 dB. The dynamic range of L-HH increased by 0.1 dB. According to the authors, a FR of 5° does not impact InSAR coherence.

Based on the discussion above, it can be assumed that the impact of FR is very small for this study. The only parameter that might be noticeably affected is L-HV backscatter. In the worst case, the slightly reduced dynamic range can result in a decreased accuracy of GSV estimation (note that the average dynamic range between dense forest and clearcuts is 3 dB; Fig. 4), thus the decrease of dynamic range will be smaller compared to the example by (Freeman & Saatchi, 2004). As the GSV estimation is conducted separately for all images by fitting an empirical model using reference data, instead of using fixed parameters for all SAR

images, potential changes of the ionospheric impact are compensated (Quegan & Lomas, 2015). Nevertheless, the slight increase of L-HV backscatter should be considered when comparing the absolute backscatter values of this study to other publications.

Due to the optimal ionospheric conditions it can be assumed that the results of this study are hardly impacted by FR. However, future L-band missions may have to deal with more severe ionospheric distortions, as the solar activity might increase and SAR acquisitions might be conducted during day time. For a first assessment of the ionospheric impact the TEC can be used and FR can be simulated as demonstrated by (Meyer & Nicoll, 2008) and (Sandberg et al., 2009). Images not suitable for the required application (Meyer, 2011) could be omitted. A more reasonable approach is to correct the distorted images. The correction requires a well calibrated SAR system (small crosstalk and channel imbalance) (Meyer, 2011; Quegan & Lomas, 2015) such as ALOS PALSAR (Rosenqvist et al., 2007; Sandberg et al., 2009) and full polarimetric data (Wright et al., 2003). Also small scale FR variations can be corrected when these preconditions are fulfilled. Therefore, low frequency full polarimetric SAR data can be used to monitor the ionospheric conditions (Meyer, 2011).

4. Methods

4.1. SAR data processing

4.1.1. Backscatter data

All SAR data were delivered in JAXA's (Japan Aerospace Exploration Agency) level 1.1 format, referring to single look complex (SLC) data in slant range geometry. The processing steps comprised radiometric calibration (Rosenqvist et al., 2007), multilooking including intensity image calculation, SRTM DEM (Shuttle Radar Topography Mission Digital Elevation Model) based orthorectification (Wegmüller, 1999) and topographic normalisation. The Gamma Software was used for this processing (Wegmüller, 1999, 2001). Regarding topographic normalisation, the pixel area correction and angular adjustment proposed by (Castel et al., 2001) was implemented.

4.1.2. INSAR data

The InSAR coherence γ is the complex correlation between two complex SAR images and consists of a phase and a magnitude component. The magnitude varies between 1 and 0, at which 1 refers to perfect correlation and 0 to no correlation. As mentioned in the introduction, the main sources of decorrelation are temporal decorrelation, volume decorrelation, and geometric decorrelation. However, two more factors can cause a degradation of InSAR coherence. These factors are the interferometer's thermal noise and the decorrelation due to non-parallel flight tracks. The impact of these factors was investigated and discussed in (Thiel & Schmullius, 2013) for the same dataset resulting in the conclusion that both thermal noise and non-parallel tracks have negligible effects on the magnitude InSAR coherence.

Interferometric processing includes SLC data co-registration to sub-pixel accuracy, slope adaptive common-band filtering in range direction to correct for geometric decorrelation (Santoro, Werner, et al., 2007; Wegmüller, 1998) and common-band filtering in azimuth direction. The interferograms were generated using 10×20 looks for FBS and 10×40 looks for FBD data. For FBD data, the number of azimuth looks was doubled to gather approximately squared pixels in ground range geometry accepting the trade-off to lose geometric resolution. The dissimilar number of independent looks resulted in a slight difference (0.03) of the zero-coherence bias (López-Martínez & Pottier, 2007; Wei & Sandwell, 2010). Thanks to the high number of independent samples, the coherence estimation bias is negligible for areas with coherence greater 0.2. The coherence images were orthorectified using SRTM elevation data. The pixel spacing of the orthorectified coherence data is $25 \text{ m} \times 25 \text{ m}$.

4.2. Approach of SAR data analysis to assess the sensitivity of backscatter and coherence for GSV

All analyses were conducted at the forest stand level. Accordingly, backscatter and coherence were averaged for each forest stand. To summarise the observations, several statistics were estimated:

- i) Average backscatter and coherence of non-forest (inventory data was used to extract all areas with a GSV of $0 \text{ m}^3/\text{ha}$, i.e. non-forest),
- ii) Average backscatter and coherence of dense forest (inventory data was used to extract all areas with a GSV between $250 \text{ m}^3/\text{ha}$ and $350 \text{ m}^3/\text{ha}$, i.e. dense forest),
- iii) GSV saturation level (using a reproducible scheme, see below),
- iv) Coefficient of determination R^2 for predicted GSV estimates, using Eqs. (1) and (2), to reference GSV values.

In many studies the saturation level is assessed visually (Table 1). This kind of assessment contains a subjective component which is hard to assess. Other studies employ mathematical functions or models to determine the saturation level. However, these functions tend to smooth the relationship between SAR data and GSV and important features can be lost. The spread is also often not considered. For these reasons we decided to apply a reproducible approach to estimate the saturation level. The details of this approach are described in Thiel and Schmullius (2013). The basic idea was to compute the separability of adjacent biomass classes (class width = $50 \text{ m}^3/\text{ha}$) starting at the lowest GSV level.

For the statistical description of the relationship between SAR data and GSV, two exponential models were applied. Eq. (1) (suggested by (Lucas et al., 2006)) was used to describe the relationship between backscatter and GSV.

$$\sigma_{GSV}^0 = \beta_s + (\beta_n - \beta_s) \cdot e^{-k \cdot GSV}. \quad (1)$$

In this equation, σ_{GSV}^0 represents the backscattering intensity [dB], GSV is the growing stock volume, β_s refers to the backscatter from forest with the highest GSV, β_n refers to the backscatter from non-forest, and k is a coefficient describing the gradient of the curve and the point of saturation.

The model formed by Eq. (2) was applied by Askne and Santoro (2005) to investigate the multitemporal variability of forest stands.

$$\gamma_{GSV} = a e^{-\frac{GSV}{c}} + b \left(1 - e^{-\frac{GSV}{c}}\right). \quad (2)$$

In Eq. (2), γ_{GSV} is the magnitude of the coherence, GSV is the growing stock volume, and a , b , and c are empirical coefficients. Indeed, a and b can be again interpreted as coherence of non-forest and forest with the highest GSV, and c describes the shape of the curve. Therefore, both models could be construed as simplified versions of the Water-Cloud Model by Attema and Ulaby (1978). The models were fit to the reference data by matching the empirical components (β_s , β_n , k , a , b , and c) using least squares estimation.

4.3. Integrative usage of SAR backscatter and coherence for the mapping of GSV

The approach of the delineation of the SAR based GSV maps can be outlined as follows (details are provided afterwards):

- i. Stratified random training data selection (20% of the forest inventory data),
- ii. Training of empirical models for HV backscatter and coherence data using least squares fitting,
- iii. Pixel based model inversion and GSV estimation,
- iv. Averaging HV backscatter and coherence GSV maps resulting in one backscatter and one coherence based GSV map,

- v. Merging the coherence and the HV backscatter GSV maps ((a) averaging, (b) elimination of areas featuring GSV difference greater 100 m³/ha, (c) setting negative values of averaged map to zero)
- vi. Assessing the accuracy of the final map using the remaining 80% of the reference data.

The stratified selection of training data is of great importance particularly for sites with a small number of forest stands, as the training of the empirical models requires training data for the whole spectrum of GSV values. The smallest number of training samples (20% of the all forest stands >2 ha) was available for Hrebtovsky NW. For this site 55 forest stands were used for model training, which can be considered a sufficiently great number of samples for training exponential models.

These six steps were applied to the sites Chunsky E, Chunsky N, Shesta, Hrebt S, and Nishni, because these sites had at least three HV backscatter images acquired in unfrozen conditions and three coherence images acquired in frozen conditions were also available. In this study, the dependency of the achieved performance on the number of available backscatter and coherence measurements was not investigated. In general, an increasing number of images results in higher accuracies of the generated GSV maps (Santoro et al., 2011). Therefore, slightly improved results can be expected when the number of measurements is increased. For each site in Siberia, on average four coherence images (temporal baseline 46 days) acquired in frozen conditions and six FBD backscatter images acquired in unfrozen conditions were available. For the delineation of the GSV, the exponential models provided with Eqs. (1) and (2) were used. Both models were fit to the training data by matching the empirical components (β_s , β_n , k , a , b , and c) using least squares method. 20% of the forest inventory data were randomly selected as training data. The model training was accomplished separately for each of the backscatter and coherence images. For the inversion Eqs. (1) and (2) were solved for GSV (Eqs. (3) & (4)).

$$GSV = \frac{\ln\left(\frac{\sigma^0 - \beta_s}{\beta_n - \beta_s}\right)}{-k} \quad (3)$$

$$GSV = -\ln\left(\frac{\gamma_{GSV} - b}{a - b}\right) \cdot c. \quad (4)$$

Eq. (3) was applied to the backscatter data and Eq. (4) to the coherence data. As unfiltered SAR data were used (only multi-looking was applied), speckle and noise are still prevalent. Consequently, the pixel wisely estimated GSV can exceed the range of the GSV training data

(e.g. (Antropov et al., 2013)). The (multitemporal) averaging of the GSV maps (steps iv.-v.) amends most of this deficiency. For the multitemporal averaging (step iv. — conducted separately for backscatter and coherence based maps) the single GSV maps were used with the same weight, as the used SAR data featured rather similar characteristics in terms of R^2 and saturation. Otherwise, weighting could be accomplished considering, for example, the difference of backscatter/coherence between forest and open areas (Santoro et al., 2011). The final merging of the backscatter and the coherence based map applied a double weight of the coherence based map, as the coherence was demonstrated being (in most cases) a better estimator for GSV. In this step, all areas featuring a GSV difference greater 100 m³/ha between the averaged backscatter and coherence based GSV map were eliminated. Eventually, all negative GSV values were set to zero.

5. Results

5.1. Potential of ALOS PALSAR InSAR coherence and backscatter for GSV estimation in central Siberia

In total, 87 ALOS PALSAR acquisitions were used and approximately 300 coherence images were delineated for GSV estimation. With regard to coherence, only the results being potentially relevant for GSV estimation are presented here. This includes the coherence images acquired in frozen conditions ($0 \text{ m} < B_{\perp} < 1800 \text{ m}$, no exclusion of interferogram based on B_{\perp}) and the coherence images acquired in unfrozen conditions with $3,100 \text{ m} < B_{\perp} < 4,100 \text{ m}$. Regarding the latter, it was found that the PALSAR coherence data with $B_{\perp} < 2,000 \text{ m}$ was not sensitive enough for estimating GSV (Thiel & Schmullius, 2013). The impact of B_{\perp} on coherence over sparse and dense forest was investigated in a previous study using the same data (Thiel & Schmullius, 2013). In frozen conditions, no impact was observed for $0 \text{ m} < B_{\perp} < 1,800 \text{ m}$. In unfrozen conditions, a slight impact between 1,000 m and 2,000 m was observed. Therefore, no subgroups featuring different perpendicular baselines were formed for this study (Fig. 4).

The majority of the coherence images had a temporal baseline of 46 days. The maximum temporal baseline was 138 days. Larger temporal baselines were omitted in order to avoid heavy temporal decorrelation. The same applies to interferograms employing data from dissimilar seasons (i.e. one image acquired in unfrozen conditions, and one image acquired in frozen conditions), as substantial decorrelation caused by the contrary environmental situation was observed (Thiel & Schmullius, 2013).

As an example, Fig. 2 shows two scatterplots demonstrating the general impact of GSV on backscatter (HV) acquired in unfrozen conditions (a) and coherence acquired in frozen conditions (b). Each of the points within the plots represents one forest stand of the inventory

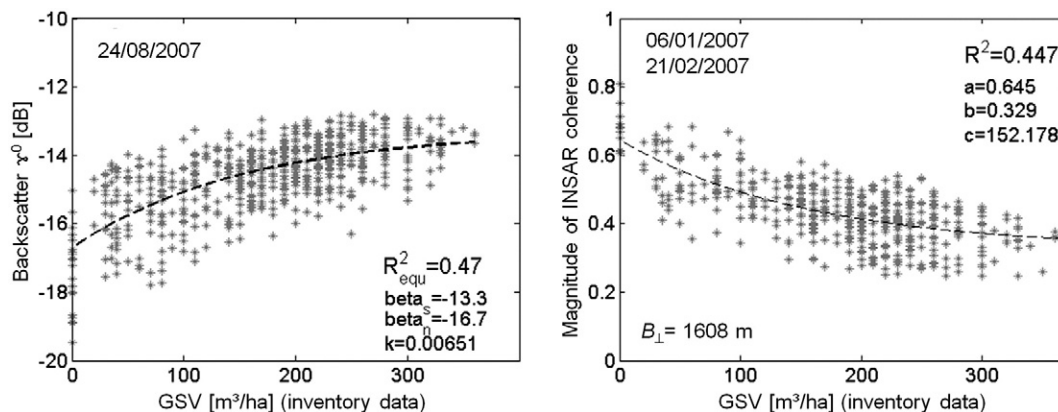


Fig. 2. Radar backscatter and coherence as function of GSV for the inventory site Hrebtovsky S. The backscatter image (HV) polarisation was acquired in unfrozen conditions, while the data for the coherence image were acquired in frozen conditions. The provided parameters define the fitted curves according to Eqs. (2) and (1).

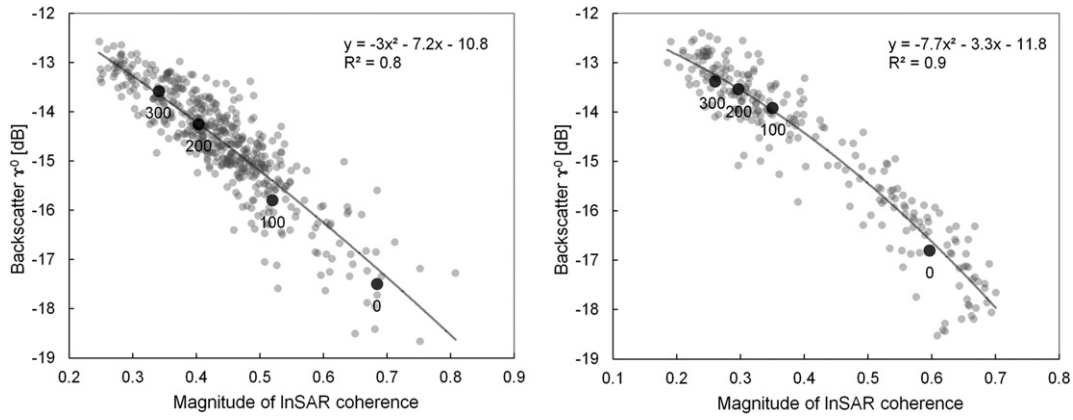


Fig. 3. Relationship between InSAR coherence and HV backscatter for (a) Hrebtovsky S and (b) Chunscky N (coherence: 05/02/2008–22/03/2008, HV backscatter: 05/08/2007) at forest stand level. Each of the small dots represents one forest stand. The four labelled points provide the average coherence and backscatter values for a GSV of 0, 100, 200, and 300 m³/ha respectively.

site Hrebtovsky S. It was observed that increased GSV resulted in increased backscatter and decreased coherence. The impact of GSV was larger at low GSV values and slightly decreased with increasing GSV.

The average backscatter of non-forest (e.g. clear-cuts, $GSV = 0 \text{ m}^3/\text{ha}$) was approximately -17 dB , while the maximum backscattering intensity was approximately -13.5 dB for dense forest ($GSV = 300 \text{ m}^3/\text{ha}$).

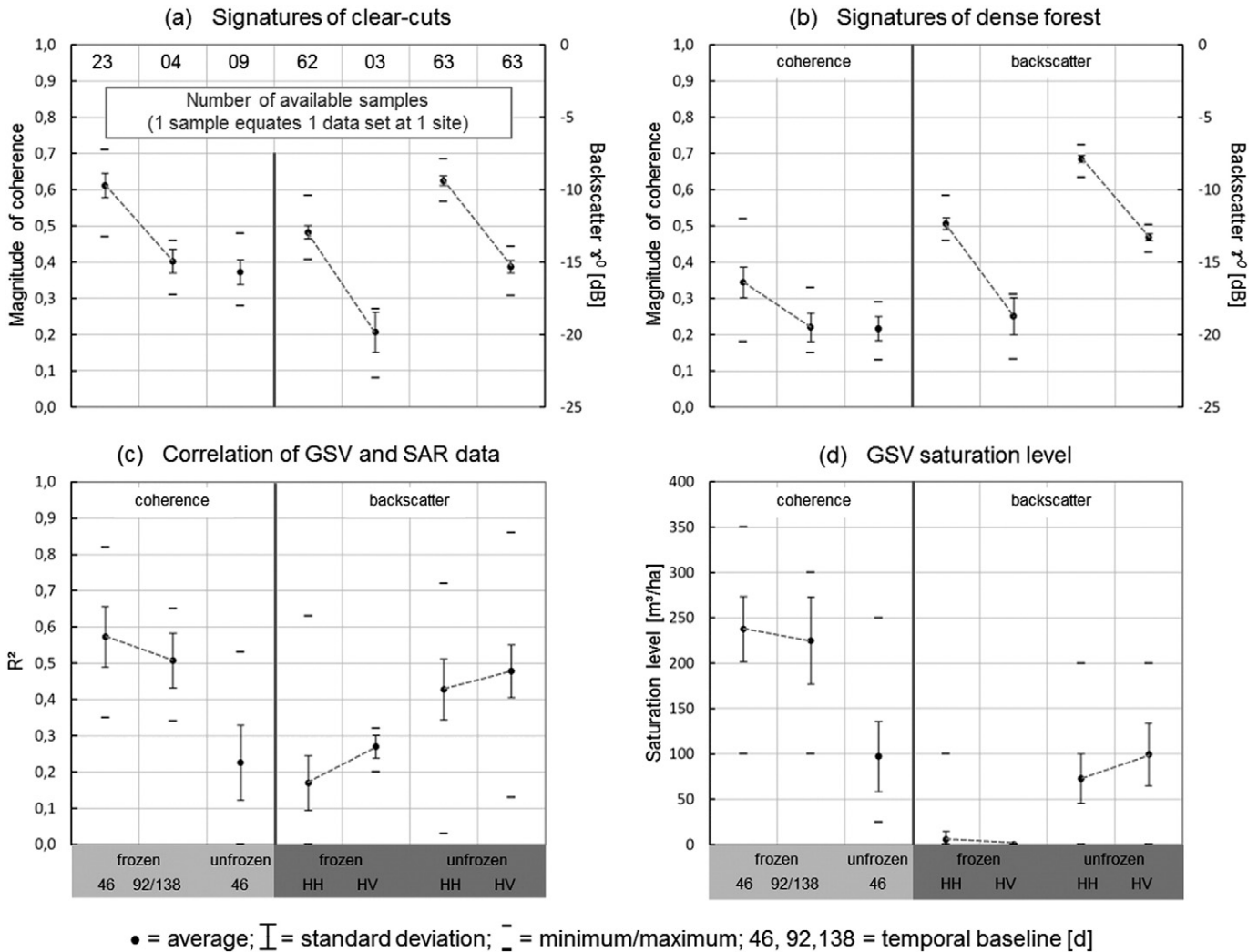


Fig. 4. Summarised results of the PALSAR data analysis for evaluating the potential regarding GSV estimation including INSAR coherence and backscatter, both acquired in frozen and unfrozen conditions. Provided are (a) the average signatures of clear-cuts, (b) the average signatures of dense forest, (c) the correlation of GSV and SAR parameter, and (d) the saturation for GSV. The statistics are separated by season, temporal baseline, and polarisation. See (a) for the number of samples. One sample refers to one backscatter/coherence image at one forest inventory site, thus each sample comprises 339–2046 forest stands.

Accordingly, the dynamic range of HV backscatter caused by different forest densities was -3.5 dB. The dynamic range of coherence was approximately 0.3. Such plots and statistics were generated for all sites and dates. Fig. 4 provides a statistical summary of the data.

Fig. 3(a) is based on the same data as Fig. 2. Fig. 3(b) provides a data example for Chunksy N. The plots for the remaining data look similar and are not provided here. Again, each point represents the average backscatter and coherence per forest stand. As discussed in the Introduction section, increasing GSV commonly results in increasing backscatter and decreasing InSAR coherence. Thus, when only forested areas were considered, a noticeable relationship between backscatter and coherence can be expected. However, as GSV is not the only factor impacting backscatter and coherence over forest, the exact degree of correlation was not assessable before this investigation. If both parameters feature a similar sensitivity for GSV, the function of the relationship will be linear. However, since coherence is expected to be more sensitive for GSV (see Section 1.1), a non-linear relationship is more likely. It should be noted that coherence and backscatter are not correlated in general. The integration of signatures for other landcover classes such as open water bodies, urban areas, or agricultural fields would introduce point clusters that are apart from the trend line (Thiel, Thiel, et al., 2009).

Overall, Fig. 3 shows a rather high correlation between backscatter and coherence. However, some points deviate noticeably from the regression line. For example, in Fig. 3(a) for a coherence value of 0.68 we found backscattering intensities from -18.5 dB to -15.5 dB and for a backscattering intensity of -17.5 dB we found coherence values from 0.81 to 0.52. As these plots (except the labelled points) were not depending on the quality of the forest inventory data, one can conclude that GSV was not the only factor impacting backscatter and coherence over forest. It is also well known (see Section 1.1) that both SAR parameters are influenced by forest structural (e.g. forest density, tree species, shape of canopy) and environmental parameters (e.g. soil moisture, canopy interception water). In areas with low GSV levels, the ground contribution is increased. Therefore, the characteristics of the ground (soil moisture, roughness, remnants of after harvest, etc.) have an increased impact on the SAR signal. Thus, over clear-cuts or over general areas featuring very low GSV, the backscatter can be very diverse. Furthermore, remaining topographic impacts can also affect backscatter and coherence.

Consequently, the GSV values from backscatter and coherence data were considerably different for forest stands that had higher residuals (Fig. 3). Using both measurements can help to avoid some of these estimation errors by excluding areas that have a large difference in backscatter and coherence based GSV values. Another option would be to simply average the intensity and coherence based maps.

The plots in Fig. 3 (and the remaining plots not provided in this paper) show a slight reduction in spread corresponding to higher GSV values. This pattern may be associated to forest density. In general, ground contribution is reduced in dense forests, meaning that soil surface (spatial variations in moisture and roughness) and topography have a weakened influence on the SAR data. Additionally, high GSV values tend to reach the limit of coherence, which can cause the coherence variations to extenuate due to the zero-coherence bias.

In Fig. 3(a), the relationship between coherence and backscatter was almost linear. Thus, the saturation level and the sensitivity for GSV were not considerably different for backscattering intensity and coherence. This observation differs somewhat from the findings based on the complete data set (comprised all eleven sites; Fig. 4), where it was observed that coherence saturation levels were significantly higher than backscatter saturation levels. Fig. 3(b) provides a better example of what was observed for most of the data set, which was that the relationship between backscatter and coherence was non-linear. The direction of the curvature of the trend line demonstrated a higher sensitivity of

coherence for GSV, which was particularly visible at high GSV values. The decreasing sensitivity of backscatter and coherence with increasing GSV was evident while observing decreasing distances between the GSV classes ($0 \text{ m}^3/\text{ha}$ – $100 \text{ m}^3/\text{ha}$, $100 \text{ m}^3/\text{ha}$ – $200 \text{ m}^3/\text{ha}$, etc.). Accordingly, the data displayed in Fig. 3(a) had a higher sensitivity for biomass compared to the Chunksy N example in Fig. 3(b).

In the following, the observations of all considered SAR data are summarised for all eleven inventory sites. Fig. 4 provides a graphical presentation of the major observations. In these four diagrams, the first three columns show the coherence data. The remaining four columns display the results based on the backscattering intensity.

All results are subdivided into frozen and unfrozen conditions. Due to the lack of an adequately dense network of meteorological stations, a further subdivision considering more detailed environmental conditions was not feasible. Regarding the backscatter data, the polarisations HH and HV were distinguished. Regarding coherence, the group frozen conditions were subdivided into two partitions to account for the increasing impact of temporal decorrelation. The first partition contains the interferograms with a temporal baseline of 46 days; the second partition features temporal baselines of 92 and 138 days. For unfrozen conditions, only interferograms with a temporal baseline of 46 days were used.

Fig. 4(a) summarises the backscatter and the coherence of clear-cuts, i.e. areas with a GSV of $0 \text{ m}^2/\text{ha}$. Therefore, low backscattering intensity and high coherence values can be expected. Diagram (b) presents the backscatter and coherence for dense forest (250 – $350 \text{ m}^3/\text{ha}$), thus high backscatter and low coherence can be expected. Commonly, the magnitude of the difference between the SAR signatures of dense forest and non-forest is related to the potential for GSV estimation: larger differences often coincide with a higher potential for GSV retrieval (Santoro et al., 2011).

Coherence acquired in frozen conditions with a temporal baseline of 46 days had the largest contrast between open areas and dense forest. The highest coherence over open areas was observed for frozen conditions with a temporal baseline of 46 days. The average value was 0.61. Dense forests had an average coherence of 0.34. In this example, the difference between open areas and dense forest was 0.27. With increasing temporal baseline the coherence decreased over both open areas and dense forest. A reduced difference of 0.19 was also observed. Given unfrozen conditions, the coherence over dense forest and open areas was similar to the coherence acquired in frozen conditions with temporal baselines of 92/138 days.

Contrary to coherence, the largest contrast of backscatter between open areas and dense forest was observed in unfrozen conditions. This contrast decreased in frozen conditions. For example, a backscattering difference of 0.2 dB in frozen and of 2.0 dB in unfrozen conditions was observed for HH polarisation. A 5 dB drop in backscatter was detected for dense forest in HH polarised images during frozen conditions. The drop was even larger for HV polarisation (6 dB). In open areas, the backscatter also decreased during frozen conditions. However, this decrease was not as large as in dense forest (HH: 3 dB, HV: 4.5 dB).

The highest R^2 values (0.51–0.58) were found for coherence acquired in frozen conditions (Fig. 4(c)). Also, there was a slight decrease of R^2 values for the large temporal baseline. The R^2 for backscattering intensity acquired in unfrozen conditions ranged from 0.42 (HH) to 0.48 (HV). The HV polarisation had a noticeably wide range of the R^2 values (0.13 to 0.87; Fig. 4(c)). For the majority, the average R^2 values of the remaining SAR data were overall very low. Coherence acquired in unfrozen conditions and backscatter acquired in frozen conditions were in general not useful for GSV estimation. Roughly the same conclusions were drawn regarding the saturation level. Saturation was reached on average between $200 \text{ m}^2/\text{ha}$ and $250 \text{ m}^2/\text{ha}$. The saturation of the backscattering intensity was reached at considerably lower GSV levels of $75 \text{ m}^2/\text{ha}$ for HH and at $100 \text{ m}^2/\text{ha}$ for HV data. Coherence acquired in unfrozen conditions had a saturation level of $100 \text{ m}^2/\text{ha}$.

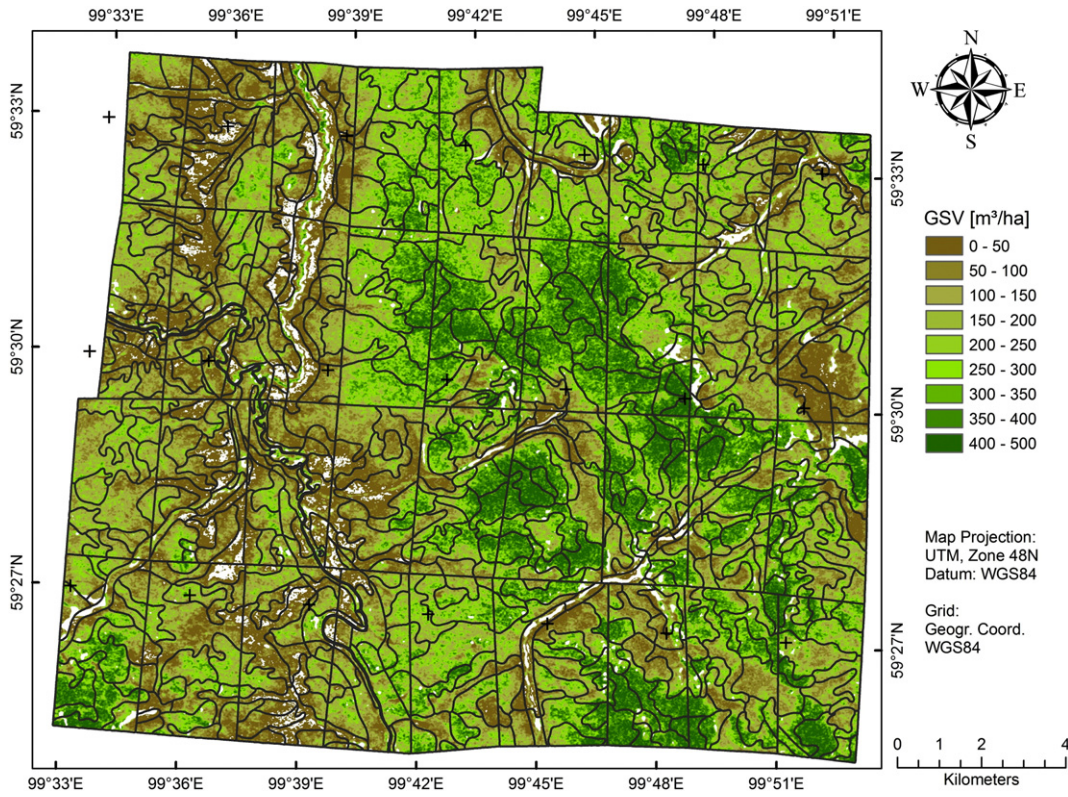


Fig. 5. GSV map of Hrebtovsky S based on 6 HV backscatter images acquired in unfrozen conditions and 3 HH coherence images acquired in frozen conditions. Information on the accuracy is provided in Fig. 6(b). The polygons encircle the forest stands.

In summary, coherence acquired in frozen conditions demonstrated the greatest potential for GSV estimation. It had the highest R^2 and the highest saturation levels. In comparison to other studies based on L-band coherence data (Table 1), higher saturation levels were identified in this study. The backscattering intensity acquired in unfrozen conditions also demonstrated some potential to estimate GSV; however, it suffers from a comparably low saturation level. Still, the radar backscatter might be useful to improve a coherence based GSV product, as discussed above in this section. The joint application of backscattering intensity and coherence for GSV estimation is demonstrated in the following paragraph.

5.2. GSV mapping results

In the following the GSV map for Hrebtovsky S (Fig. 5) as well as the accuracy statistics for the other four chosen test sites derived using the procedure described in Section 4.3 are discussed. For the delineation of the GSV map, three coherence images and six HV backscatter images were available. The average R^2 between coherence and GSV was 0.44. This value is rather low when compared to Fig. 4(c). The saturation level was determined at 250 m^3/ha . The average R^2 between HV backscatter and GSV was 0.48, which corresponds quite well to the average of all investigated sites. The HV backscatter was found to saturate at

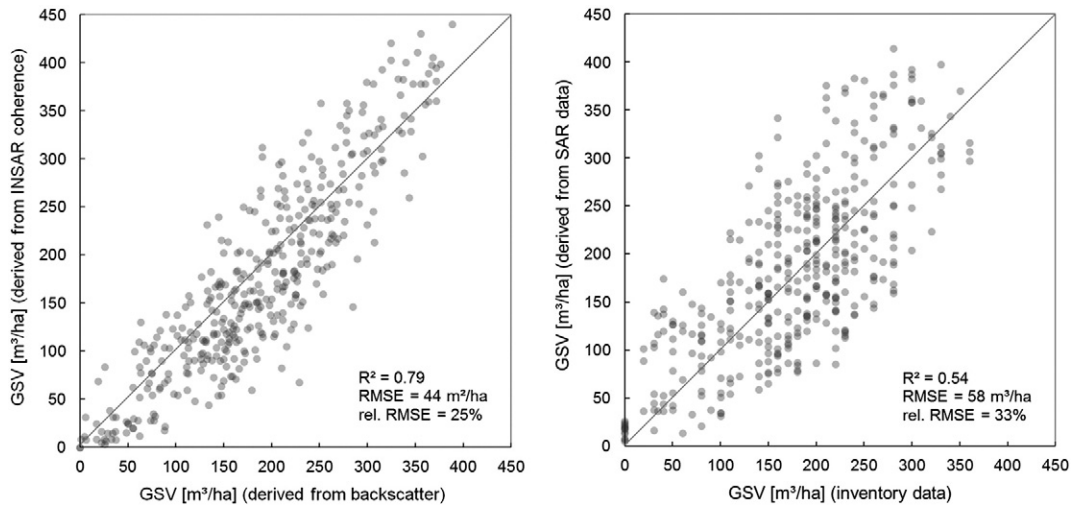


Fig. 6. (a) Forest stand level based comparison of two SAR data based GSV maps for Hrebtovsky S; (b) Forest stand level based comparison of inventory data and the final SAR data based GSV map.

200 m³/ha, which is a high value compared to the average of 100 m³/ha (Fig. 4).

It was observed in the GSV map (Fig. 5) that patches featuring no-data (referring to eliminated data, see Section 4.3) were primarily found next to areas with a low GSV, which was usually located in floodplains. This finding is in agreement with the observations provided with Fig. 3, where forest stands that had low backscatter and high coherence (i.e. the forest stands with the presumably lowest GSV) also had the highest spread. One potential reason for this observation is the high sensitivity of the SAR backscatter to soil moisture during unfrozen conditions. In particular, the soil moisture in floodplains is typically high, sometimes they are even flooded. Therefore, high backscatter can occur in areas with sparse forest. During frozen conditions, the impact of soil moisture changes is reduced, which would explain why a high coherence was found. On the other hand, decorrelation can be caused by forest management activities taking place in open areas such as clear-cuts. These activities may include the transportation of wood, the removal of debris or the installation of local infrastructure for the forestry management sector. Although this kind of change causes decorrelation, the impact on the backscatter can be rather low. Therefore, by eliminating areas that have a GSV difference between the backscatter and coherence based GSV map greater than 100 m³/ha, some errors related to the above issues can be avoided.

The accuracy of the final maps was evaluated with the remaining 80% of the reference data. For this step, R² and RMSE were computed. To be precise, the RMSE should be treated as root mean square deviation between forest inventory data and the SAR based GSV map, as the inventory data itself has an RMSE_{inv} of 15%–20%.

There was generally good agreement between forest stand level GSV derived from backscatter and coherence when compared to the forest inventory GSV data (Fig. 6(a)). An overall bias was not observed. For the comparison of GSV estimates of backscatter to coherence data, an R² of 0.79 was found and a relative RMSE of 25% was observed. The averaging of backscatter and coherence GSV maps helped to reduce the spread at low GSV levels. Yet, backscatter and coherence GSV were spread around the 1:1 line; meaning that the usage of either backscatter or coherence could introduce an under- or overestimation of GSV.

In comparison to the forest inventory, a marginal improvement in the proportion of variance (R² = 0.54) in GSV estimation accounted for by the combination of coherence and backscatter data was observed (Fig. 6(b)). This is relative to the individual performances of coherence (R² = 0.50) and backscatter (R² = 0.51) to estimate GSV. The relative RMSE of the combined data was 33%, which was slightly lower than observed individually for coherence (37%) and backscatter (36%) data. Thus, the synergistic usage of backscatter and coherence may not only be useful for determining exclusion criteria for areas with considerable GSV differences, but also it may have some potential to improve SAR-based GSV estimations.

As reported above, the relative RMSE between inventory data and the final PALSAR based GSV was 33%. If independence is assumed for the SAR based estimation error RMSE_{sar} and the inventory estimation error RMSE_{inv}, a corrected RMSE_{corr} of the final PALSAR based GSV map can be computed: $RMSE_{corr} = (RMSE_{sar}^2 - RMSE_{inv}^2)^{0.5}$. Accordingly, the relative RMSE_{corr} for Hrebtovsky S lies between 26% and 29%. Thus, the final PALSAR based map features an accuracy which was close to the accuracy of the forest inventory data. Compared to previous work in

this field of science (Table 1), this result corresponds to the studies reporting the higher accuracies.

Table 4 provides *rel. RMSE_{corr}* and R² for all five sites. Except for Chunksy N, the *rel. RMSE_{corr}* was below 30%. The reason for the rather high error value for Chunksy N lies in the comparably low average GSV of this site (a high percentage of Chunksy N was harvested or in some stage of regrowth), the absolute RMSE for Chunksy N was similar to the other sites.

6. Summary and conclusions

The study investigates the capability of L-band backscatter and coherence for the estimation of GSV in Siberia using a large amount of PALSAR data. It was observed that coherence acquired in frozen conditions offers the largest potential for GSV estimation. For single images, the saturation occurs in average at 230 m³/ha, the R² between coherence and GSV (based on Eq. (2)) was 0.58 on average. Comparable results were found in other studies (Table 1) using ERS-1/2 Tandem data. Results based on JERS-1 coherence had lower saturation levels (Eriksson et al., 2003). PALSAR backscatter also had some sensitivity to GSV estimation. However, saturation occurred at lower GSV levels (75–100 m³/ha). Also, the average R² was lower (0.42–0.48). Regarding L-band backscatter, slightly lower GSV saturation levels and coefficients of determination compared to other studies was observed (Antropov et al., 2013; Kurvonen et al., 1999; Rauste, 2005). Overall, HV backscatter offered a slightly greater potential than HH backscatter for GSV estimation.

GSV maps were generated and validated for five sites. For the delineation of the map coherence data acquired in frozen conditions and backscatter data acquired in unfrozen conditions were used. The delineation was based on a rather simple and straight forward approach that could be operationally applied over large areas. This approach does not consider potential change within the time series of acquisitions. Areas featuring change such as new clear-cuts could be detected, e.g. by computing multitemporal metrics using the backscatter images (Thiel et al., 2009). The training of the GSV retrieval algorithms was based on forest inventory data. One requirement of the conventional forest inventory data is that it comprises the whole range of appearing GSV levels. If no inventory data are available, the usage of other products, such as the MODIS Vegetation Continuous Fields (Hansen et al., 2003), may be applied for the model training (Cartus, Santoro, Schmullius, Yong, & Zengyuan, 2007; Santoro et al., 2011). Another successfully applied training approach is based on the analysis of the image statistics of SAR data (Askne & Santoro, 2009; Wagner et al., 2003).

In general, the produced maps feature a corrected relative RMSE_{corr} of <30%. This figure assumes an RMSE of 20% of the inventory data. Thus, the final PALSAR based map features an accuracy which is close to the accuracy of the forest inventory data itself. Compared to previous work in this field of science (Table 1), this result corresponds to studies reporting the higher accuracies.

The approach is based on a suited PALSAR data set with regard to the acquisition conditions. It was found that frozen conditions are crucial for qualifying InSAR coherence to be used as estimator for GSV. If meteorological data are available, the environmental conditions for the time of the acquisition time can be examined before data processing and unsuited image pairs can be avoided. For the case of meteorological data being unavailable the coherence data can be analysed, as image pairs acquired at dissimilar conditions (frozen/unfrozen) of a thaw event at one of the acquisition dates become manifest in significantly reduced coherence over open areas (Thiel & Schmullius, 2013). Therefore, a straight forward strategy would be to exclude those image pairs by applying a coherence threshold for open areas.

In summary, it could be demonstrated that ALOS PALSAR data have the potential to map the GSV of the Siberian forest with an accuracy of the conventional forest inventory data. Thanks to the sophisticated observation strategy (Rosenqvist et al., 2007) and the high acquisition

Table 4
Accuracy assessment of the predicted GSV for the sites Chunksy E, Chunksy N, Shesta, Hrebt S, and Nishni.

	Chunksy E	Chunksy N	Shesta	Hrebt S	Nishni
No. of images	5/5	5/6	6/3	6/3	4/3
backscatter/coherence					
<i>rel. RMSE_{corr}</i> [%]	59.0	29.8	28.5	26.0	28.3
R ²	0.79	0.79	0.54	0.57	0.83

success rate in that area, on average four coherence images (temporal baseline 46 days) for each site in Siberia were acquired in frozen conditions and six FBD backscatter images acquired in unfrozen. The results of this study might gather some particular importance with regard to ESA's forthcoming earth explorer mission BIOMASS, as for a great partition of the boreal zone (Northern America, Northern Europe) P-band acquisitions may not/or only partly be permitted.

Acknowledgements

This work has been undertaken [in part] within the framework of the JAXA Kyoto & Carbon Initiative. ALOS PALSAR data have been provided by JAXA EORC. The authors thank all reviewers and editors for their valuable comments and suggestions. Special thanks go to Jason Goetz for proofreading the manuscript.

References

- (IPCC), I.P.o.C.C. (2003). *Good practice guidance for land use, land-use change and forestry, IPCC National Greenhouse Gas Inventories Programme UNEP*. Kyoto Miwa: Institute for Global Environmental Strategies (IGES).
- Ackermann, N., Thiel, C., Borgeaud, M., & Schmullius, C. (2012). Cosmo-skymed backscatter intensity and interferometric coherence signatures over Germany's low mountain range forested areas. *IGARSS (Munich, Germany)*.
- Ahmed, R., Siqueira, P., Hensley, S., Chapman, B., & Bergen, K. (2011). A survey of temporal decorrelation from spaceborne L-band repeat-pass InSAR. *Remote Sensing of Environment*, 115, 2887–2896.
- Antropov, O., Rauste, Y., Ahola, H., & Häme, T. (2013). Stand-level stem volume of boreal forests from spaceborne SAR imagery at L-band. *IEEE Journal of Selected Topics in Applied Earth Observations and Remote Sensing*, 6, 35–44.
- Askne, J., & Santoro, M. (2005). Multitemporal repeat pass SAR interferometry of boreal forests. *IEEE Transactions on Geoscience and Remote Sensing*, 43, 1219–1228.
- Askne, J., & Santoro, M. (2007). Boreal forest stem volume estimation from multitemporal C-band InSAR observations. *ESA Envisat Symposium* (Montreux, Switzerland).
- Askne, J., & Santoro, M. (2009). Automatic model-based estimation of boreal forest stem volume from repeat pass C-band InSAR coherence. *IEEE Transactions on Geoscience and Remote Sensing*, 47, 513–516.
- Askne, J., Santoro, M., Smith, G., & Fransson, J. E. S. (2003). Multitemporal repeat-pass SAR interferometry of boreal forests. *IEEE Transactions on Geoscience and Remote Sensing*, 41, 1540–1550.
- Askne, J. I. H., Fransson, J. E. S., Santoro, M., Soja, M. J., & Ulander, L. M. H. (2013). Model-based biomass estimation of a hemi-boreal forest from multitemporal TanDEM-X acquisitions. *Remote Sensing*, 5, 5574–5597.
- Attema, E. P. W., & Ulaby, F. T. (1978). Vegetation modeled as a water cloud. *Radio Science*, 13, 357–364.
- Balster, H., Talmon, E., Wagner, W., Gaveau, D., Plummer, S., Yu, J. J., ... Schmullius, C. (2002). Accuracy assessment of a large-scale forest cover map of central Siberia from synthetic aperture radar. *Canadian Journal of Remote Sensing*, 28, 719–737.
- Baranchikov, Y. N. (2011). Siberian moth – A relentless modifier of Taiga forest ecosystems in Northern Asia. In E. A. Vaganov (Ed.), *IBFRA – Boreal forests in a changing world: Challenges and needs for actions* (pp. 105–107). Krasnoyarsk, Russia: Sukachev Institute of Forests.
- Carreiras, J. M. B., Vasconcelos, M. J., & Lucas, R. M. (2012). Understanding the relationship between aboveground biomass and ALOS PALSAR data in the forests of Guinea-Bissau (West Africa). *Remote Sensing of Environment*, 121, 426–442.
- Cartus, O., Santoro, M., & Kellndorfer, J. (2012). Mapping forest aboveground biomass in the northeastern United States with ALOS PALSAR dual-polarization L-band. *Remote Sensing of Environment*, 124.
- Cartus, O., Santoro, M., Schmullius, C., Yong, P., & Zengyuan, L. (2007). Creation of large area forest biomass maps for NE China using ERS-1/2 tandem coherence. *ESA Envisat Symposium* (Meontreux, Switzerland).
- Castel, T., Beaudoin, A., Stach, A., Stussi, N., LeToan, T., & Durand, P. (2001). Sensitivity of space-borne SAR data to forest parameters over sloping terrain. Theory and experiment. *International Journal of Remote Sensing*, 22, 2351–2376.
- Castel, T., Guerra, F., Caraglio, Y., & Houllier, F. (2002). Retrieval biomass of a large Venezuelan pine plantation using JERS-1 SAR data. Analysis of forest structure impact on radar signature. *Remote Sensing of Environment*, 79, 30–41.
- Castel, T., Martínez, J. M., Beaudoin, A., Wegmuller, U., & Strozzi, T. (2000). ERS INSAR data for remote sensing hilly forested areas. *Remote Sensing of Environment*, 73, 73–86.
- Cuevas-González, M., Gerard, F., Balster, H., & Riano, D. (2009). Analysing forest recovery after wildfire disturbance in boreal Siberia using remotely sensed vegetation indices. *Global Change Biology*, 1–17.
- Del Frate, F., & Solimini, D. (2004). On neural network algorithms for retrieving forest biomass from SAR data. *IEEE Transactions on Geoscience and Remote Sensing*, 42, 24–34.
- Disney, M., Lewis, P., & Saich, P. (2006). 3D modelling of forest canopy structure for remote sensing simulations in the optical and microwave domains. *Remote Sensing of Environment*, 100, 114–132.
- Dobson, M. C. (1988). Diurnal and seasonal variations in the microwave dielectric constant of selected trees. In T. D. Guyenne, & J. J. Hunt (Eds.), *IEEE international geoscience and remote sensing symposium IGARSS* (pp. 1754). Edinburgh, U.K.: ESA Publications Division.
- Dobson, M. C., Ulaby, F. T., Le Toan, T., Beaudoin, A., Kasischke, E. S., & Christensen, N. (1992). Dependence of radar backscatter on coniferous forest biomass. *IEEE Transactions on Geoscience and Remote Sensing*, 30, 412–415.
- Dobson, M. G., McDonald, K., & Ulaby, F. T. (1990). Effects of temperature on radar backscatter from boreal forests. In R. Mills (Ed.), *IEEE international geoscience and remote sensing symposium IGARSS* (pp. 2481–2484). College Park, Maryland, USA: IEEE Publications.
- Eriksson, L. E. B., Santoro, M., & Fransson, J. E. S. (2008). Temporal decorrelation for forested areas observed in spaceborne L-band SAR interferometry. In S. C. Reising, & D. Entekhabi (Eds.), *IEEE international geoscience and remote sensing symposium IGARSS* (pp. 283–285). Boston, Massachusetts, U.S.A.: IEEE Publications.
- Eriksson, L. E. B., Santoro, M., Wiesmann, A., & Schmullius, C. C. (2003). Multitemporal JERS repeat-pass coherence for growing-stock volume estimation of Siberian forest. *IEEE Transactions on Geoscience and Remote Sensing*, 41, 1561–1570.
- Eriksson, L. E. B., Schmullius, C. C., & Wiesmann, A. (2004). Temporal decorrelation of spaceborne L-band repeat-pass coherence. In M. Zink (Ed.), *Parameters from SAR Data for Land Applications BioGeoSAR* (pp. CD-ROM). Innsbruck, Austria: ESA Publications Division.
- Fraser, R. H., & Li, Z. (2002). Estimating fire-related parameters in boreal forest using SPOT VEGETATION. *Remote Sensing of Environment*, 82, 95–110.
- Fraser, R. H., Li, Z., & Cihlar, J. (2000). Hotspot and NVDI differencing synergy (HANDS): A new technique for burned area mapping over boreal forest. *Remote Sensing of Environment*, 74, 362–376.
- Freeman, A., & Saatchi, S. S. (2004). On the detection of Faraday rotation in linearly polarized L-band SAR backscatter signatures. *IEEE Transactions on Geoscience and Remote Sensing*, 42, 1607–1616.
- Gatelli, F., Guarnieri, A. M., Parizzi, F., Pasquali, P., Prati, C., & Rocca, F. (1994). The wave-number shift in SAR interferometry. *IEEE Transactions on Geoscience and Remote Sensing*, 32, 855–865.
- Gaveau, D. L. A. (2002). Modelling the dynamics of ERS-1/2 coherence with increasing woody biomass over boreal forests. *International Journal of Remote Sensing*, 23, 3879–3885.
- Gullison, R. E., Frumhoff, P. C., Canadell, J. G., Field, C. B., Nepstad, D. C., Hayhoe, K., ... Nobre, C. (2007). Environment. Tropical forests and climate policy. *Science*, 316, 985–986.
- Hagberg, J., Ulander, L. M. H., & Askne, J. (1995). Repeat-pass SAR interferometry over forested terrain. *IEEE Transactions on Geoscience and Remote Sensing*, 33, 331–340.
- Häme, T., Salli, A., & Lahti, K. (1992). Estimation of carbon storage in boreal forests using remote sensing data. In M. Kanninen, & P. Anttila (Eds.), *The Finnish research program on climate change* (pp. 250–255). Helsinki: Academy of Finland.
- Hansen, M. C., De Fries, R. S., Townshend, J. R. G., Carroll, M., Dimiceli, C., & Sohlberg, R. A. (2003). Global percent tree cover at a spatial resolution of 500 meters: first results of the MODIS vegetation continuous field algorithm. *Earth Interactions*, 7, 1–15.
- Harrell, P. A., Kasischke, E. S., BourgeauChavez, L. L., Haney, E. M., & Christensen, N. L. (1997). Evaluation of approaches to estimating aboveground biomass in southern pine forests using SIR-C data. *Remote Sensing of Environment*, 59, 223–233.
- Healey, S. P., Cohen, W. B., Yang, Z. Q., & Krankina, O. N. (2005). Comparison of Tasseled Cap-based Landsat data structures for use in forest disturbance detection. *Remote Sensing of Environment*, 97, 301–310.
- Israelsson, H., Askne, J., & Sylvander, R. (1994). Potential of SAR for forest bole volume estimation. *International Journal of Remote Sensing*, 15, 2809–2826.
- Israelsson, H., Ulander, L. M. H., Martin, T., & Askne, J. I. H. (2000). A coherent scattering model to determine forest backscattering in the VHF-band. *IEEE Transactions on Geoscience and Remote Sensing*, 38, 238–248.
- Joshi, N., Mitchard, E., Schumacher, J., Johannsen, V., Saatchi, S., & Fensholt, R. (2015). L-band SAR backscatter related to forest cover, height and aboveground biomass at multiple spatial scales across Denmark. *Remote Sensing*, 7, 4442–4472.
- Kasischke, E. S., BourgeauChavez, L. L., French, N. H. F., Harrell, P., & Christensen, N. L. (1992). Initial observations on using SAR to monitor wildfire scars in boreal forests. *International Journal of Remote Sensing*, 13, 3495–3501.
- Kellndorfer, J. M., Dobson, M. C., Vona, J. D., & Clutter, M. (2003). Toward precision forestry: plot-level parameter retrieval for slash pine plantations with JPL AIRSAR. *IEEE Transactions on Geoscience and Remote Sensing*, 41, 1571–1582.
- Kimes, D. S., Ranson, K. J., & Sun, G. (1997). Inversion of a forest backscatter model using neural networks. *International Journal of Remote Sensing*, 18, 2181–2199.
- Kononov, A. A., & Ka, M. H. (2008). Model-associated forest parameter retrieval using VHF SAR data at the individual tree level. *IEEE Transactions on Geoscience and Remote Sensing*, 46, 69–84.
- Koskinen, J. T., Pulliainen, J. T., Hyypää, J. M., Engdahl, M. E., & Hallikainen, M. T. (2001). The seasonal behavior of interferometric coherence in boreal forest. *IEEE Transactions on Geoscience and Remote Sensing*, 39, 820–829.
- Kurvonen, L., Pulliainen, J., & Hallikainen, M. (1999). Retrieval of biomass in boreal forests from multitemporal ERS-1 and JERS-1 SAR images. *IEEE Transactions on Geoscience and Remote Sensing*, 37, 198–205.
- Kwok, R., Rignot, E. J. M., Way, J., Freeman, A., & Holt, J. (1994). Polarization signatures of frozen and thawed forests of varying environmental state. *IEEE Transactions on Geoscience and Remote Sensing*, 32, 371–381.
- Lang, R. H., Chauhan, N. S., Ranson, K. J., & Kilic, O. (1994). Modeling P-band SAR returns from a red pine stand. *Remote Sensing of Environment*, 47, 132–141.
- Lavalle, M., Simard, M., & Hensley, S. (2012). A temporal decorrelation model for polarimetric radar interferometers. *IEEE Transactions on Geoscience and Remote Sensing*, 2880–2888, 7.
- Liang, P., Moghaddam, M., Pierce, L. E., & Lucas, R. M. (2005). Radar backscattering model for multilayer mixed-species forests. *IEEE Transactions on Geoscience and Remote Sensing*, 43, 2612–2626.

- López-Martínez, C., & Pottier, E. (2007). Coherence estimation in synthetic aperture radar data based on speckle noise modeling. *Applied Optics*, 46, 544–558.
- Lozano, F. J., Suarez-Seoane, S., Kelly, M., & Luis, E. (2008). A multi-scale approach for modeling fire occurrence probability using satellite data and classification trees: A case study in a mountainous Mediterranean region. *Remote Sensing of Environment*, 112, 708–719.
- Lucas, R. M., Cronin, N., Lee, A., Moghaddam, M., Witte, C., & Tickle, P. (2006). Empirical relationships between AIRSAR backscatter and LIDAR-derived forest biomass, Queensland, Australia. *Remote Sensing of Environment*, 100, 407–425.
- Lucas, R. M., Moghaddam, M., & Cronin, N. (2004). Microwave scattering from mixed-species forests, Queensland, Australia. *IEEE Transactions on Geoscience and Remote Sensing*, 42, 2142–2159.
- Luckman, A., Baker, J., Kuplich, T. M., Yanasse, C. D. F., & Frery, A. C. (1997). A study of the relationship between radar backscatter and regenerating tropical forest biomass for spaceborne SAR instruments. *Remote Sensing of Environment*, 60, 1–13.
- Luckman, A., Baker, J., & Wegmuller, U. (2000). Repeat-pass interferometric coherence measurements of disturbed tropical forest from JERS and ERS satellites. *Remote Sensing of Environment*, 73, 350–360.
- McDonald, K. C., Zimmermann, R., & Kimball, J. S. (2002). Diurnal and spatial variation of xylem dielectric constant in Norway spruce (*Picea abies* [L.] karst.) as related to microclimate, xylem sap flow, and xylem chemistry. *IEEE Transactions on Geoscience and Remote Sensing*, 40, 2063–2082.
- Melon, P., Martinez, J. M., Le Toan, T., Ulander, L. M. H., & Beaudoin, A. (2001). On the retrieving of forest stem volume from VHF SAR data: Observation and modeling. *IEEE Transactions on Geoscience and Remote Sensing*, 39, 2364–2372.
- Meyer, F. J. (2011). Performance requirements for ionospheric correction of low-frequency SAR data. *IEEE Transactions on Geoscience and Remote Sensing*, 49, 3694–3702.
- Meyer, F. J., & Nicoll, J. B. (2008). Prediction, detection, and correction of faraday rotation in full-polarimetric L-band SAR data. *IEEE Transactions on Geoscience and Remote Sensing*, 46, 3076–3086.
- Michelaklis, D., Stuart, N., Broly, M., Woodhouse, I. H., Lopez, G., & Linares, V. (2015). Estimation of woody biomass of pine savanna woodlands from ALOS PALSAR imagery. *IEEE Journal of Selected Topics in Applied Earth Observations and Remote Sensing*, 8, 244–254.
- Mitchard, E. T. A., Saatchi, S. S., Woodhouse, I. H., Nangendo, G., Ribeiro, N. S., Williams, M., ... Meir, P. (2009). Using satellite radar backscatter to predict above-ground woody biomass: A consistent relationship across four different African landscapes. *Geophysical Research Letters*, 36, 1–6.
- NASA (2014). Solar mini-max. In T. Phillips (Ed.), *Science news*. NASA: Washington.
- Neumann, M., Saatchi, S. S., Ulander, L. M. H., & Fransson, J. E. S. (2012). Assessing performance of L- and P-band polarimetric interferometric SAR data in estimating boreal forest above-ground biomass. *IEEE Transactions on Geoscience and Remote Sensing*, 50, 714–726.
- Nguyen, H., Roussel, H., & Tabbara, W. (2006). A coherent model of forest scattering and SAR imaging in the VHF and UHF-band. *IEEE Transactions on Geoscience and Remote Sensing*, 44, 838–848.
- Papathanassiou, K. P., & Cloude, S. R. (2001). Single-baseline polarimetric SAR interferometry. *IEEE Transactions on Geoscience and Remote Sensing*, 39, 2352–2363.
- Peterson, L. K., Bergen, K. M., Brown, D. G., Vashchuck, L., & Blam, Y. (2009). Forested land-cover patterns and trends over changing forest management eras in the Siberian Baikal region. *Forest Ecology and Management*, 257, 911–922.
- Pinto, N., Simard, M., & Dubayah, R. (2012). Using InSAR coherence to map stand age in a boreal forest. *Remote Sensing*, 5, 42–56.
- Praks, J., Antropov, O., & Hallikainen, M. (2012). LIDAR-aided SAR interferometry studies in boreal forest: scattering phase center and extinction coefficient at X- and L-band. *IEEE Transactions on Geoscience and Remote Sensing*, 50, 3831–3843.
- Pulliainen, J., Engdahl, M., & Hallikainen, M. (2003). Feasibility of multi-temporal interferometric SAR data for stand-level estimation of boreal forest stem volume. *Remote Sensing of Environment*, 85, 397–409.
- Pulliainen, J. T., Kurvonen, L., & Hallikainen, M. T. (1999). Multitemporal behavior of L- and C-band SAR observations of boreal forests. *IEEE Transactions on Geoscience and Remote Sensing*, 37, 927–937.
- Quegan, S., & Lomas, M. R. (2015). The interaction between faraday rotation and system effects in synthetic aperture radar measurements of backscatter and biomass. *IEEE Transactions on Geoscience and Remote Sensing*, 53, 4299–4312.
- Ranson, K. J., & Sun, G. (2000). Effects of environmental conditions on boreal forest classification and biomass estimates with SAR. *IEEE Transactions on Geoscience and Remote Sensing*, 38, 1242–1252.
- Rauste, Y. (2005). Multi-temporal JERS SAR data in boreal forest biomass mapping. *Remote Sensing of Environment*, 97, 263–275.
- Rignot, E., Salas, W. A., & Skole, D. L. (1997). Mapping deforestation and secondary growth in Rondonia, Brazil, using imaging radar and thematic mapper data. *Remote Sensing of Environment*, 59, 167–179.
- Rignot, E. J. M. (2000). Effect of faraday rotation on L-band interferometric and polarimetric synthetic-aperture radar data. *IEEE Transactions on Geoscience and Remote Sensing*, 38, 383–390.
- Robinson, C., Saatchi, S., Neumann, M., & Gillespie, T. (2013). Impacts of spatial variability on aboveground biomass estimation from L-band radar in a temperate forest. *Remote Sensing*, 5, 1001–1023.
- Rosenqvist, A., Shimada, M., Ito, N., & Watanabe, M. (2007). ALOS PALSAR: A pathfinder mission for global-scale monitoring of the environment. *IEEE Transactions on Geoscience and Remote Sensing*, 45, 3307–3316.
- Saatchi, S. S., & Moghaddam, M. (2000). Estimation of crown and stem water content and biomass of boreal forest using polarimetric SAR imagery. *IEEE Transactions on Geoscience and Remote Sensing*, 38, 697–709.
- Sandberg, G., Eriksson, L. E. B., & Ulander, L. M. H. (2009). Measurements of Faraday rotation using polarimetric PALSAR images. *IEEE Transactions on Geoscience and Remote Sensing Letters*, 6, 142–146.
- Sandberg, G., Ulander, L. M. H., Fransson, J. E. S., Holmgren, J., & Le Toan, T. (2011). L- and P-band backscatter intensity for biomass retrieval in hemiboreal forest. *Remote Sensing of Environment*, 115, 2874–2886.
- Sandberg, G., Ulander, L. M. H., Wallerman, J., & Fransson, J. E. S. (2014). Measurements of forest biomass change using P-band synthetic aperture radar backscatter. *IEEE Transactions on Geoscience and Remote Sensing*, 52, 6047–6061.
- Santorio, M., Shvidenko, A., McCallum, I., Askne, J., & Schmullius, C. (2007a). Properties of ERS-1/2 coherence in the Siberian boreal forest and implications for stem volume retrieval. *Remote Sensing of Environment*, 106, 154–172.
- Santorio, M., Werner, C., Wegmüller, U., & Cartus, O. (2007b). Improvement of interferometric SAR coherence estimates by slope-adaptive range common band filtering. In A. Camps, A. Broquetas, & A. Comerón (Eds.), *IEEE international geoscience and remote sensing symposium IGARSS* (pp. 129–132). Barcelona, Spain: IEEE Publications.
- Santorio, M., Askne, J., Smith, G., & Fransson, J. E. S. (2002). Stem volume retrieval in boreal forests from ERS-1/2 interferometry. *Remote Sensing of Environment*, 81, 19–35.
- Santorio, M., Beer, C., Cartus, O., Schmullius, C., Shvidenko, A., McCallum, I., ... Wiesmann, A. (2011). Retrieval of growing stock volume in boreal forest using hyper-temporal series of envisat ASAR ScanSAR backscatter measurements. *Remote Sensing of Environment*, 115, 490–507.
- Santorio, M., Eriksson, L., Askne, J., & Schmullius, C. (2006). Assessment of stand-wise stem volume retrieval in boreal forest from JERS-1 L-band SAR backscatter. *International Journal of Remote Sensing*, 27, 3425–3454.
- Santorio, M., Eriksson, L., & Fransson, J. E. S. (2015). Reviewing ALOS PALSAR backscatter observations for stem volume retrieval in Swedish forest. *Remote Sensing*, 7, 4290–4317.
- Santorio, M., Fransson, J. E. S., Eriksson, L. E. B., Magnusson, M., Ulander, L. M. H., & Olsson, H. (2009). Signatures of ALOS PALSAR L-band backscatter in Swedish forest. *IEEE Transactions on Geoscience and Remote Sensing*, 47, 4001–4019.
- Santos, J. R., Freitas, C. C., Araujo, L. S., Dutra, L. V., Mura, J. C., Gama, F. F., ... Sant'Anna, S. J. S. (2003). Airborne P-band SAR applied to the aboveground biomass studies in the Brazilian tropical rainforest. *Remote Sensing of Environment*, 87, 482–493.
- Sarabandi, K., & Lin, Y. C. (2000). Simulation of interferometric SAR response for characterizing the scattering phase center statistics of forest canopies. *IEEE Transactions on Geoscience and Remote Sensing*, 38, 115–125.
- Simard, M., Hensley, S., Laval, M., Dubayah, R., Pinto, N., & Hofton, M. (2012). An empirical assessment of temporal decorrelation using the uninhabited aerial vehicle synthetic aperture radar over forested landscapes. *Remote Sensing*, 4, 975–986.
- Smith, G., & Ulander, L. M. H. (1998). *2nd Int. Workshop on retrieval of Bio- and Geophysical Parameters from SAR data for land applications*. ESTEC, Noordwijk, NL: ESA.
- Smith, G., & Ulander, L. M. H. (2000). A model relating VHF-band backscatter to stem volume of coniferous boreal forest. *IEEE Transactions on Geoscience and Remote Sensing*, 38, 728–740.
- Smith-Jonforsen, G., Ulander, L. M. H., & Luo, X. Y. (2005). Low VHF-band backscatter from coniferous forests on sloping terrain. *IEEE Transactions on Geoscience and Remote Sensing*, 43, 2246–2260.
- Sun, G., & Ranson, K. J. (1995). A three-dimensional radar backscatter model of forest canopies. *IEEE Transactions on Geoscience and Remote Sensing*, 33, 372–382.
- Sun, G., Ranson, K. J., & Kharuk, V. I. (2002). Radiometric slope correction for forest biomass estimation from SAR data in the Western Sayani Mountains, Siberia. *Remote Sensing of Environment*, 79, 279–287.
- Tansey, K. J., Luckman, A. J., Skinner, L., Balzter, H., Strozzi, T., & Wagner, W. (2004). Classification of forest volume resources using ERS tandem coherence and JERS backscatter data. *International Journal of Remote Sensing*, 25, 751–768.
- Thiel, C., & Schmullius, C. (2013). Investigating ALOS PALSAR interferometric coherence in central Siberia at unfrozen and frozen conditions: implications for forest growing stock volume estimation. *Canadian Journal of Remote Sensing*, 39, 232–250.
- Thiel, C., Cartus, O., Eckhardt, R., Richter, N., Thiel, C., & Schmullius, C. (2009a). Analysis of multi-temporal land observation at C-band. *IEEE International Geoscience and Remote Sensing Symposium IGARSS* (pp. CD-ROM) (Cape Town, Republic of South Africa).
- Thiel, C., Thiel, C., Reiche, J., Leiterer, R., & Schmullius, C. (2007). Analysis of ASAR and PALSAR data for optimising forest cover mapping. In M. Deshayes (Ed.), *ForestSat* (pp. CD-ROM). Montpellier, France: Cemagref - France.
- Thiel, C. J., Thiel, C., & Schmullius, C. C. (2009b). Operational large-area forest monitoring in Siberia using ALOS PALSAR summer intensities and winter coherence. *IEEE Transactions on Geoscience and Remote Sensing*, 47, 3993–4000.
- Townsend, P. A. (2002). Estimating forest structure in wetlands using multitemporal SAR. *Remote Sensing of Environment*, 79, 288–304.
- Treuhaf, R., Gonçalves, F., Santos, J. R. d., Keller, M., Palace, M., Madsen, S. N., ... Graça, P. M. L. A. (2015). Tropical-forest biomass estimation at X-band from the spaceborne TanDEM-X interferometer. *IEEE Transactions on Geoscience and Remote Sensing Letters*, 12, 239–244.
- Ulaby, F., Sarabandi, K., McDonald, K., Whitt, M., & Dobson, C. (1990). Michigan microwave canopy scattering model (MIMICS). *International Journal of Remote Sensing*, 11, 1123–1253.
- Varekamp, C., & Hoekman, D. H. (2002). High-resolution InSAR image simulation for forest canopies. *IEEE Transactions on Geoscience and Remote Sensing*, 40, 1648–1655.
- Villard, L., & LeToan, T. (2015). Relating P-band SAR intensity to biomass for tropical dense forests in hilly terrain: γ_0 or t_0 . *IEEE Journal of Selected Topics in Applied Earth Observations and Remote Sensing*, 8, 214–223.
- Wagner, W., Luckman, A., Vietmeier, J., Tansey, K., Balzter, H., Schmullius, C., ... Yu, J. J. (2003). Large-scale mapping of boreal forest in Siberia using ERS tandem coherence and JERS backscatter data. *Remote Sensing of Environment*, 85, 125–144.

- Wang, Y., Paris, J. F., & Davis, F. W. (1998). Inclusion of a simple multiple scattering model into a microwave canopy backscatter model. *Remote Sensing of Environment*, 63, 101–111.
- Watanabe, M., Shimada, M., Rosenqvist, A., Tadono, T., Matsuoka, M., Romshoo, S. A., ... Moriyama, T. (2006). Forest structure dependency of the relation between L-band σ_0 and biophysical parameters. *IEEE Transactions on Geoscience and Remote Sensing*, 44, 3154–3165.
- Way, J., Paris, J., Kasischke, E., Slaughter, C., Viereck, L., Christensen, N., ... Weber, J. (1990). The effect of changing environmental-conditions on microwave signatures of forest ecosystems — Preliminary-results of the March 1988 Alaskan aircraft SAR experiment. *International Journal of Remote Sensing*, 11, 1119–1144.
- Way, J., Rignot, E. J. M., McDonald, K. C., Oren, R., Kwok, R., Bonan, G., ... Roth, J. E. (1994). Evaluating the type and state of Alaska taiga forests with imaging radar for use in ecosystem models. *IEEE Transactions on Geoscience and Remote Sensing*, 32, 353–370.
- Wegmüller, U. (1998). SAR interferometric and differential interferometric processing. In T. I. Stein (Ed.), *IEEE international Geoscience and Remote Sensing Symposium IGARSS* (pp. 1106–1108). Seattle, USA: IEEE Publications.
- Wegmüller, U. (1999). Automated terrain corrected SAR geocoding. *IGARSS* (Hamburg, Germany).
- Wegmüller, U. (2001). Automated and precise image registration procedures. *First International Workshop on Multitemp 2001* (pp. 37–49). Italy: University of Trento.
- Wei, M., & Sandwell, D. T. (2010). Decorrelation of L-band and C-band interferometry over vegetated areas in California. *IEEE Transactions on Geoscience and Remote Sensing*, 48, 2942–2952.
- White, J. C., Wulder, M. A., Brooks, D., Reich, R., & Wheate, R. D. (2005). Detection of red attack stage mountain pine beetle infestation with high spatial resolution satellite imagery. *Remote Sensing of Environment*, 96, 340–351.
- Wright, P. A., Quegan, S., Wheadon, N. S., & Hall, C. D. (2003). Faraday rotation effects on L-band spaceborne SAR data. *IEEE Transactions on Geoscience and Remote Sensing*, 41, 2735–2744.
- Yanasse, C. D. F., SantAnna, S. J. S., Frery, A. C., Renno, C. D., Soares, J. V., & Luckman, A. J. (1997). Exploratory study of the relationship between tropical forest regeneration stages and SIR-C L and C data. *Remote Sensing of Environment*, 59, 180–190.
- Yatabe, S. M., & Leckie, D. G. (1995). Clearcut and forest-type discrimination in satellite SAR imagery. *Canadian Journal of Remote Sensing*, 21, 456–467.
- Zan, F. D., Krieger, G., & López-Dekker, P. (2013). On some spectral properties of TanDEM-X interferograms over forested areas. *IEEE Transactions on Geoscience and Remote Sensing Letters*, 10, 71–76.